Available online at www.sciencedirect.com
SCIENCE DIRECT®
C. R. Physique 6 (2005) 525–547
COMPTES RENDUS PHYSIQUE
http://france.elsevier.com/direct/COMREN/

Aircraft trailing vortices/Tourbillons de sillages d'avions

Interaction of exhaust jets and aircraft wake vortices: small-scale dynamics and potential microphysical-chemical transformations

Roberto Paoli [a,*], François Garnier [b]

[a] *CERFACS, 42, avenue Gaspard Coriolis, 31057 Toulouse cedex, France*
[b] *ONERA-DMPH, 29, avenue de la Division Leclerc, 92320 Châtillon cedex, France*

Available online 5 July 2005

Abstract

This paper summarizes recent progress made in the understanding of the interaction between exhaust jets and trailing vortices, in the near field of an aircraft wake. Emphasis is placed on the effects of the jet on the wake vortex dynamics and the effects of the wake on the exhaust dispersion, as well as their potential microphysical and chemical transformations. We discuss in detail results of high-resolution numerical simulations of jet/vortex interaction that include microscale turbulent mixing, gas-phase chemistry and contrail formation. ***To cite this article: R. Paoli, F. Garnier, C. R. Physique 6 (2005).***

Résumé

Interaction entre un jet propulsif et un tourbillon de sillage d'avions : dynamique à petite échelle et transformations physico-chimiques. Ce papier décrit les progrès récents concernant l'étude de l'interaction entre les jets propulsifs et les tourbillons de sillage, dans le champ proche d'un avion de transport. Une attention particulière a été portée sur les effets des jets sur la dynamique des tourbillons de sillage et l'influence des ces derniers à la fois sur la dispersion des émissions aussi bien que sur les transformations microphysiques et chimiques, qui peuvent avoir un impact sur l'environnement. Nous discutons les résultats de simulations numériques basées sur des approches DNS et LES, de la dynamique et du mélange à petite échelle ainsi que les transformations chimiques et la formation des traînées de condensation. ***Pour citer cet article : R. Paoli, F. Garnier, C. R. Physique 6 (2005).***

Keywords: Wake vortex; Exhaust jet; DNS; LES; Contrails; Chemical transformations

Mots-clés : Tourbillon de sillage ; Jet propulsif ; DNS ; LES ; Traînées de condensation ; Transformations chimiques

1. Introduction

The interaction between aircraft wake vortices and exhaust jets is a subject of academic research and practical interest in many areas of aerospace science and technology. Examples range from the characterization of the structure of hazardous trailing vortices during take-off and landing and the development of new concepts to accelerate their decay (see Spalart [1]), to the investigation of the environmental impact of aircraft emissions. The latter represents the main motivation of the present

* Corresponding author.
E-mail addresses: Roberto.Paoli@cerfacs.fr (R. Paoli), Francois.Garnier@onera.fr (F. Garnier).

1631-0705/$ – see front matter
doi:10.1016/j.crhy.2005.05.003

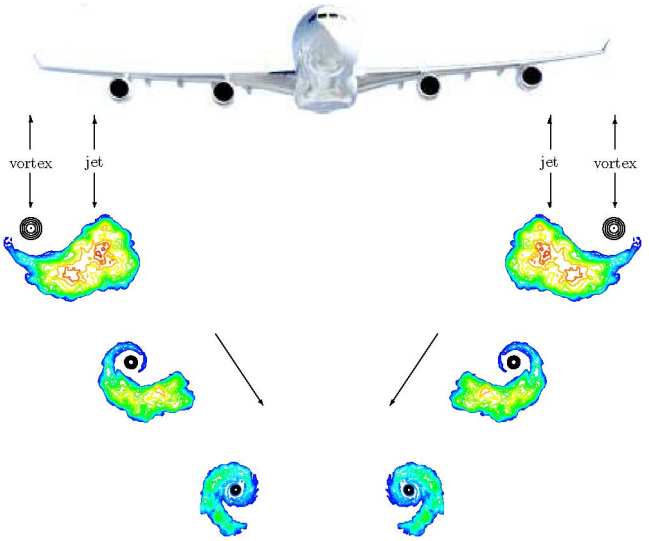

Fig. 1. Basic configuration of a jet/vortex interaction in the near field of an aircraft wake.

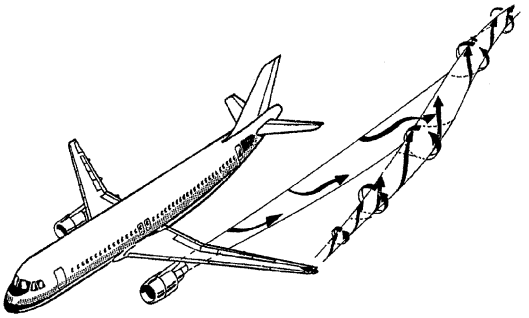

Fig. 2. Sketch of the jet and interaction regimes.

work and has been assessed in the IPCC (Intergovernmental Panel on Climate Change) special report of 1999 [2], where some key topics were identified that need further investigation. Gaseous emissions like CO_2, NO_x and SO_x alter the concentration of atmospheric greenhouse gases; particles resulting from incomplete combustion like soot, trigger the formation of condensation trails (contrails), artificially increasing cloudiness and altering climate (see Fahey and Schumann [3]). Besides these global effects, emissions like CO or CH_4 emitted by the engines are trapped by aircraft trailing vortices in very localized zones thus contributing to air pollution around the airports. These specific issues have been mostly addressed in geophysical and atmospheric sciences, through in situ measurements [4,5] or numerical simulations with different levels of complexity [6,7]. The main intent was to characterize the general features of the exhaust plumes diffusion, on length-scales up to kilometers from the engine and time-scales up to minutes from the emission time. On the other hand, very few papers can be found in the literature that analyze in detail the interaction of an engine jet and a trailing vortex in the near field of the wake (see Fig. 1). This is a basic step to the understanding of how the exhausts mix with ambient air during the first seconds after the emission and the influence of the vortex wake in this process. At the same time, it is useful to evaluate the local effects of 'single-aircraft' emissions on the atmospheric environment, and provide inputs to climate or environmental investigations.

The qualitative features of the jet/vortex interaction were first illustrated by Hoshizaki et al. [8] and later by Miake-Lye et al. [9] who identified two distinct phases. During the first few seconds after emission, the jets rapidly mix with ambient air (jet regime) while the vorticity shed from the wings rolls up into a pair of trailing vortices. Later on, the dynamics is dominated by the entrainment of the jets into the vortex flow (interaction regime, see Fig. 2). One of the earliest experimental studies on this topic is due to El-Ramy and Rainbird [10], in the context of aircraft-wake hazard concern at terminal operation. They found that the engine exhausts did not appreciably influence the wing-tip structure but had significantly altered the shear layer instability coming off the trailing edge of the wing. Brunet et al. [11] presented an experimental study to characterize the dynamics of the jet in the vortex wake of a scaled model, representative of a large transport aircraft in cruise conditions. The laser lightsheet visualization revealed that part of the jet was already entrained at a distance of only one-half wingspan downstream. Seiner et al. [12] analyzed the influence of vortex-wake and pylon-wake on high-speed subsonic round jet, with a focus on aeroacoustic implications. Both experiments and simulations showed that the jet evolved into a non-circular structure and they inferred that it would probably generate a non-symmetric noise field as well. Wang et al. [13,14] performed experimental studies of a coflowing jet immersed in the vortex wake of a delta-wing platform. An important outcome of these studies was that the jet produced additional vortices as a consequence of being immersed in the induced velocity field of the vortex wake. The action of all these vortices caused a lateral stretching and a vertical compression of the jet and ultimately led to a quicker velocity decay, compared to the baseline coflowing jet with the same velocity ratio. If this ratio is sufficiently high, the jet turbulence can spread the vortex core as shown in the experiments by Kantha et al. [15] and Phillips and Graham [16]. On the other hand, Huppertz et al. [17] investigated the very near wake up to five chord lengths behind the trailing edge of a rectangular wing and analyzed different engine positions and jet speed. They observed that the jet did not significantly alter the tangential velocity distribution of the vortex but modified the streamwise component of the velocity which is relevant for the evaluation of axial stresses. An interesting attempt to simulate the jet/vortex sheet interaction in a realistic aircraft flow geometry was

recently done by Fares et al. [18] with a sophisticated Reynolds averaged Navier–Stokes solver, keeping, however, the intrinsic limitations of steady flow assumption. Other authors focused on the analysis of the vortex decay in atmospheric turbulence or in sheared/stratified environments, using numerical simulations with different level of sophistication, from vortex filaments models [19] to two-dimensional DNS [20] and LES [21] (see also Holzapfel et al. [22] and references therein).

Looking at the jet and wake-vortex interaction requires previous knowledge on the generic dynamics of jets and aircraft wakes. Jet profiles are known to be unstable, with a robust instability mechanism of Kelvin-Helmoltz type. By using the normal modes approach, Michalke and Herman [23] provided the exact growth rates of the instability of a simple axisymmetric jet developing spatially in an inviscid incompressible flow. Brancher [24] performed a linear analysis for the same jet developing temporally, and completed the analysis for viscous flows with spectral numerical simulations. Loiseleux et al. [25] and Lu and Lele [26] extended the analysis to swirling flows, respectively for jets and wakes and for mixing layers. The characteristics of real engine jets may be significantly different from the academic jet flows studied within the framework of the linear stability theory. As shown by Freund et al. [27,28], at high subsonic convective Mach numbers around 0.8–0.9 encountered in modern commercial aircrafts, compressibility alters the structure of the exhaust scalar field as well as the pressure field which is crucial for the prediction of sound radiated by the jet (see also Freund et al. [29] and Freund [30]). Heating increases axial mixing and entrainment of jets by cold external air through density gradients, as shown, for instance, by Ricou and Spalding [31] who measured increased entrainment rates for hydrogen jets and Abramovich et al. [32] who measured larger axial vortex decay and mixing for low density ratios S_ρ, between jet and air flows. The density ratio also affects jet stability, indeed Monkewitz and Sohn [33] found that the jet becomes absolutely unstable when S_ρ is reduced below 0.72.

The wake structure of an aircraft in the near to mid-field (less than 50 wing-spans behind the aircraft) may be different depending on the flight phase and the type of aircraft (see e.g. the reviews of Spalart [1] and Rossow [34]). The aircraft sheds a vorticity sheet at the trailing edge of the lifting surface, which rolls-up into a small number of concentrated vortices at a distance of about one wing-span behind the aircraft. On cruise flight, the vorticity sheet shed by one wing essentially rolls up into a single vortex, emanating from the wing tip. For both two- or four-engine aircrafts, the jets are produced far from the initial vortex position. The complete wake is composed by a counter-rotating vortex pair in this case. In high-lift configurations the wake shed by one wing may roll up into several co- or counter-rotating vortices, depending on the flap setting. These vortices interact in the near to mid-field, which often results in the merging of the co-rotating structures and the formation of a single vortex pair in the far-field, as it is the case for cruise flight conditions. In these configurations, the jet/vortex sheet interaction is more complex than in cruise flight, since, for example, four-engine aircrafts may generate jets in the vicinity of the flap vortex. Regions of combined rotational fluid and axial velocity may be considered as swirling jets or as vortices with axial velocity (‘q’-vortices, see Batchleor [35]) and are known to be unstable under certain conditions (Mayer and Powell [36], Ragab and Sreedhar [37], Hu et al. [38]). Several other instability mechanisms have also been demonstrated in the literature, such as the classical long-wave Crow instability (Lewellen and Lewellen [39], Lewellen et al. [40], Rennich and Lele [41]), the short-wave elliptical instability (Leweke et al. [42], Le Dizès and Laporte [43]) and the four-vortex Crouch-type instability (Crouch [44], Fabre and Jacquin [45]). Characterization studies have also brought detailed knowledge on the wake vortex structure (Devenport et al. [46,47], Chen et al. [48], Jacquin et al. [49], Fabre [50], Laporte [51]) either for cruise or high-lift configurations.

The goal of the present work is to give a short survey of some recent studies that have been carried out on the jet/vortex interaction problem. Focus is laid on the analysis of the interaction occurring in simple academic configurations such as between a jet and a single trailing vortex (Section 2). Two environmental applications are then discussed in Section 3, i.e. the alteration of the chemical composition and the formation of a contrail in an aircraft wake, respectively. Conclusions are finally given in Section 4.

2. Dynamics and mixing in jet/vortex interactions

The results described in this section are mostly based on the direct numerical simulations (DNS) and large-eddy simulations (LES) recently performed by Ferreira Gago et al. [52] and Paoli et al. [53], respectively. These authors used finite difference solvers where spatial discretization and time integration were performed by means of a sixth-order compact scheme by Lele [54] and a three-stage Runge–Kutta method, respectively. Non-reflecting boundary conditions by Poinsot and Lele [55] were used for all non-periodic directions.

Both [52] and [53] report temporal simulations, i.e. the computational box is convected downstream with the air-flow velocity u_∞ (e.g. the aircraft or the experimental model velocity) so that the distance d from the aircraft is translated into a temporal delay from the emission time, i.e. $d = u_\infty \times t$ (and periodic boundary conditions can be used in the axial direction of the box). This is based on the assumption of locally parallel flow which means that the gradients of the mean flow in the axial direction are neglected over the short distance corresponding to the axial dimension of the simulation domain (see e.g. Gaster [56]). The instabilities developing in this way are automatically of convective nature, so that absolute instabilities cannot be captured. However, the Kelvin-Helmoltz instability developing in jet flows has been shown to be convective (see Brancher [24] and references therein), and the 3D temporal simulation approach has been validated for academic flows, as mixing layers or jets [24,38,57].

Furthermore, some authors like Michalke and Hermann [23] and Cortesi et al. [58] showed that numerical simulations based on the time-dependent approach could be a useful tool for interpreting turbulence phenomena if some restrictions are applied.

Another assumption made by [52] and [53] is to split the simulations in two sequential phases that correspond to the two regimes identified by Miake-Lye et al. [9]: (i) the jet regime, when the jets rapidly mix with ambient air while the wing-generated vorticity sheet rolls up into a pair of trailing vortices; and (ii) the deflection regime, when the dynamics is dominated by the entrainment of the jets into the wake vortex. This assumption is not straightforward looking at the complex flow behind an aircraft. Nevertheless, the distance for roll-up completion is of the order of one aircraft span, which corresponds to tens of jet exit radii. As the jet is expected to become fully turbulent over a distance of the order of ten jet radii, the well-formed vortex interacts with a turbulent jet. Therefore, it is assumed that the jet base flow is not strongly modified (jet profile stretching) by the vortex sheet during the characteristic time scale of the jet instability. An evaluation of these time scales made by Paoli et al. [53] showed that during the time taken by the jet to travel one initial jet radius (with the velocity induced by the vortex), the amplitude of the jet instability has grown approximately of a factor e. During this time, the differential effects of the vortex induced velocity on the initially axisymmetric jet profile (corrugation effects) are expected to be very weak. A maximum differential displacement of the core of the order of 3% of the jet radius was observed in [53], validating a posteriori this approach.

2.1. Direct numerical simulations and comparison with experiments

The characteristic dimensions of the numerical set-up are provided by a wind tunnel experiment and are based on similarity parameters of a large transport aircraft with two engine jets. This experimental study detailed in Brunet et al. [59] delivers a database that can be used for improving such computational approaches. The wake of a generic model corresponding to a rectangular plan form NACA0012 equipped with two heated jets is investigated (see Fig. 3). The experimental results include mean and fluctuating velocity fields (measured with a LDV system) and mean temperature field (measured with thermocouples); the apparatus can also provide hot wire measurements. The experimental results show that the vortex flow does not affect the engine jet behaviour until a downstream distance of 0.5–1 b, b being the wingspan. For modern large transport aircraft, the characteristic size of the jet regime is of the order of 1–50 diameters of the nozzle exit, while the deflection regime extends downstream of the airplane up to a distance of about 1–10 b.

Temporal DNS were performed for the 3D compressible Navier–Stokes equations, which in dimensionless form are

$$\frac{\partial \rho}{\partial t} + \frac{\partial (\rho u_j)}{\partial x_j} = 0 \tag{1}$$

$$\frac{\partial (\rho u_i)}{\partial t} + \frac{\partial (\rho u_i u_j)}{\partial x_j} + \frac{\partial p}{\partial x_i} = \frac{1}{Re} \frac{\partial \tau_{ij}}{\partial x_j} \tag{2}$$

$$\frac{\partial (\rho E)}{\partial t} + \frac{\partial [(\rho E + p) u_j]}{\partial x_j} = \frac{1}{Re} \frac{\partial (u_i \tau_{ij})}{\partial x_j} - \frac{1}{Re\, Pr} C_p \frac{\partial q_j}{\partial x_j} \tag{3}$$

where the non-dimensional variables are: the density ρ, the velocity vector (u_1, u_2, u_3), the pressure p, the total energy E, the heat flux vector (q_1, q_2, q_3) given by Fourier's law, and the shear stress tensor τ_{ij}. The C_p coefficient is the specific heat at constant pressure. The non-dimensional variables are defined as the local dimensional variables divided by a reference variable or a combination of the reference variables. The reference variables are: the density ρ_{ref}, the velocity a_{ref}, the pressure p_{ref}, the length l_{ref}, the temperature T_{ref}, the dynamic viscosity μ_{ref} and the specific heat $C_{p,\text{ref}}$. The reference Reynolds number is $Re = a_{\text{ref}} l_{\text{ref}} / (\mu_{\text{ref}} / \rho_{\text{ref}})$ while Pr is the Prandtl number. Mixing is studied through the passive scalar transport equation:

$$\frac{\partial (\rho Y)}{\partial t} + \frac{\partial (\rho Y u_j)}{\partial x_j} = \frac{1}{Re\, Sc} \frac{\partial}{\partial x_j} \left(\mu \frac{\partial Y}{\partial x_j} \right) \tag{4}$$

where Y is the scalar mass fraction, and Sc denotes the Schmidt number; in the present simulation $Pr = Sc = 0.75$ which gives a Lewis number $Le = Sc/Pr = 1$. The simulation is performed in two phases: during the jet regime the computational domain

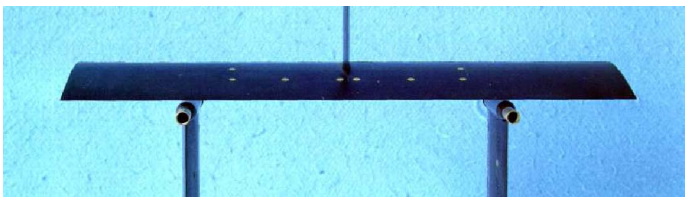

Fig. 3. Typical model used in the experimental study of the jet/vortex interaction (from [59]).

is $L_x = 6r_j$ and $L_y = L_z = 11r_j$, being r_j the nozzle-exit radius, with a total of 137×137 grid points in the cross-plane and 61 in the axial direction. The axial length of the domain corresponds to twice the wavelength of the maximum growth rate of the first azimuthal instability of a spatially evolving jet [23]. A tanh nozzle-exit profile is prescribed for axial velocity and for passive scalar,

$$u_0(r) = \frac{1}{2}u_j\left\{1 - \tanh\left[\frac{1}{4}\frac{r_j}{\theta}\left(\frac{r}{r_j} - \frac{r_j}{r}\right)\right]\right\}, \qquad Y_0(r) = \frac{1}{2}\left\{1 - \tanh\left[\frac{1}{4}\frac{r_j}{\theta}\left(\frac{r}{r_j} - \frac{r_j}{r}\right)\right]\right\} \tag{5}$$

where r is the radial coordinate in a cross-section, while the Reynolds number based on the jet centerline velocity u_j and the jet radius is $Re_j = u_j r_j/\nu = 1000$. In order to trigger the jet instability and its transition to turbulence, a three-dimensional random perturbation field is added to $u_0(r)$. When the jet simulation has reached an age that corresponds to a downstream distance of 0.5 wing spans ($d/b = 0.5$), the cross-section of the domain is enlarged and a Lamb–Oseen vortex is superimposed on the flow field at a distance of 14 vortex core radii from the jet center, as detailed in [52] (see also Figs. 4(b) and 5(a)). The cross-section domain in this phase is $L_y = L_z = 20r_j$ with 327×327 grid points. The tangential velocity profile of the vortex is given by a Lamb–Oseen model while pressure is obtained by integration of the axisymmetric momentum equation,

$$v_\theta(r) = \alpha v_c \frac{r_c}{r}\left(1 - \mathrm{e}^{-\beta r^2/r_c^2}\right), \qquad \frac{\mathrm{d}p}{\mathrm{d}r} = \rho\frac{v_\theta^2}{r} \tag{6}$$

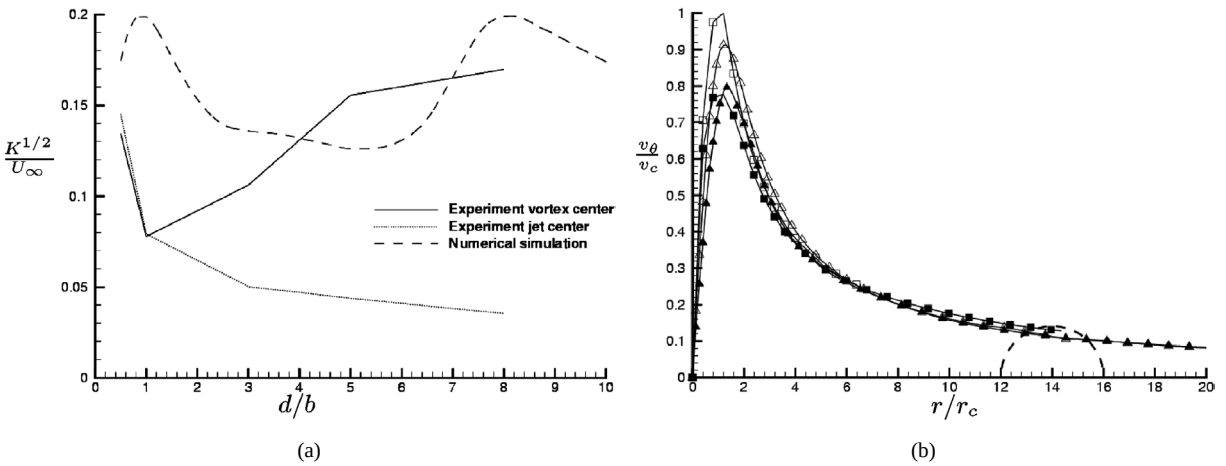

(a) (b)

Fig. 4. Evolution of the jet/vortex interaction. (a) Downstream evolution of the total turbulent kinetic energy. (b) Computational Lamb–Oseen vortex fit of the experimental velocity field at $d/b = 0.5$ (△) and $d/b = 8$ (□): hollow symbols, experimental results; filled symbols, DNS. The dashed circle shows the diameter and the initial position of the jet relative to the vortex center, $r/r_c \simeq 14$, as provided by the experimental data (from [52]).

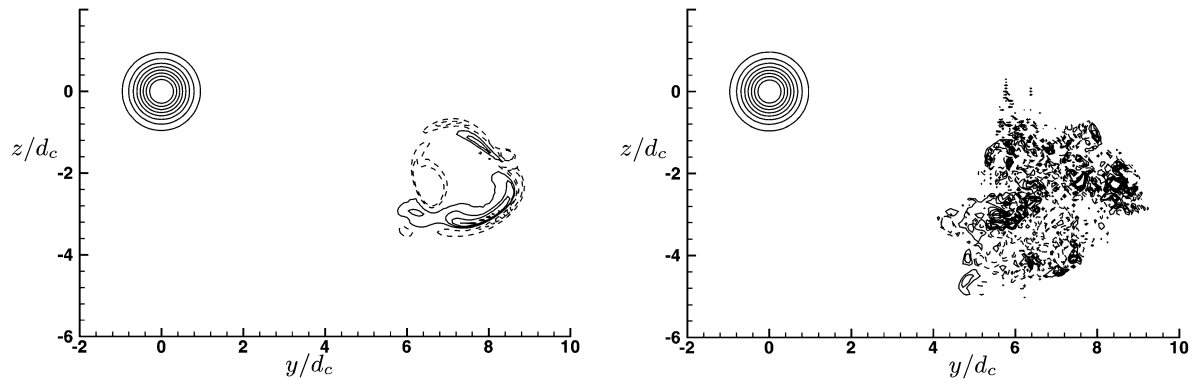

(a) (b)

Fig. 5. Normalized axial vorticity contours in a vertical lateral cross-section at (a) $d/b = 0.5$ and (b) $d/b = 1$. Dashed lines denote negative vorticity; contours range from -1 to 4 in steps of 0.5 (from [52]).

where $\alpha = 1.4$ and $\beta = 1.2544$, while v_c denotes the maximum tangential velocity at the core radius r_c. The ratio of the jet radius at the nozzle exit and the initial vortex core radius amounts to $r_j/r_c = 1.3$ and the ratio of the maximum jet and tangential velocities at $d/b = 0.5$ to $u_j/v_c = 2.72$. In all cases, time is normalized by the vortex time scale, $t_c = 2r_c/v_c = d_c/v_c$, i.e. $t^* = t/t_c$. Here it is set zero at the beginning of the second simulation when the jet has reached an age of $t^* = 9$. The conversion of time to downstream distance is established employing the Taylor assumption with the experimental freestream velocity $u_\infty = 2.2\,v_c$, i.e. $d/b = (u_\infty\, t_c\, t^*)/b$. Fig. 4(a) shows the downstream evolution of the turbulent kinetic energy (obtained by summing over all wavenumbers the one-dimensional spectrum). Thus, kinetic energy can be expressed only as a function of time (or spatial location). The turbulence rates measured by LDV in the jet centerline and in the vortex center are also reported. Examining the evolution of turbulent kinetic energy provided by the computations, one could identify three stages. During the first stage, which covers a downstream distance between $d/b \simeq 0.5$ and $d/b \simeq 6$, kinetic energy initially increases up to $d/b = 1$, mainly due to the growth of the most unstable mode. This is shown in Fig. 5 which reports the cross-sections of axial vorticity at $d/b = 0.5$ and $d/b = 1$, respectively. At the center of the computational domain (i.e. $x/d_c = 0$ and $z/d_c = 0$), positive and concentric contours represent the vorticity distribution of the vortex core. The presence of the most unstable (i.e. most energetic) mode within the jet is highlighted in Fig. 5(a), where the longitudinal component of vorticity is relatively well organized into positive and negative fields, respectively. As long as the energy increases up to the station $d/b = 1$, the vorticity field keeps its coherency as shown by the appearance of large-scale structures. These unstable structures burst subsequently and the jet reaches a fully turbulent state at $d/b = 1$ (see Fig. 5(b)). In the experiment, the jet is already fully turbulent at $d/b = 0.5$. Then, no comparison with experimental data can be made between $d/b = 0.5$ and $d/b = 1$. As shown in Fig. 4(a), the kinetic energy undertakes then to decrease until 3 wingspans downstream. A similar trend is observed for the turbulent rate measured at the center of the jet. The energy fall is probably accelerated by the presence of the rotational component of the vortex field. This first stage characterizes the tangential velocity influence of the vortex upon the jet development. Until $d/b = 6$, the vortex core does not move. Indeed, the turbulent jet field does not affect the Lamb–Oseen model.

In the second stage, between stations $d/b = 6$ and $d/b = 8$, the vortex center starts to oscillate in the cross planes, with maximum amplitude of the order of $\delta r = 1/3d_c$ (not shown). This oscillatory motion has also been observed experimentally by Devenport et al. [47] and seems to be related to the influence of the turbulence generated by the jet flow upon the vortex behavior. Finally, in the third stage, beyond 8 wingspan downstream, the turbulent kinetic energy saturates, and then a period of decay sets in.

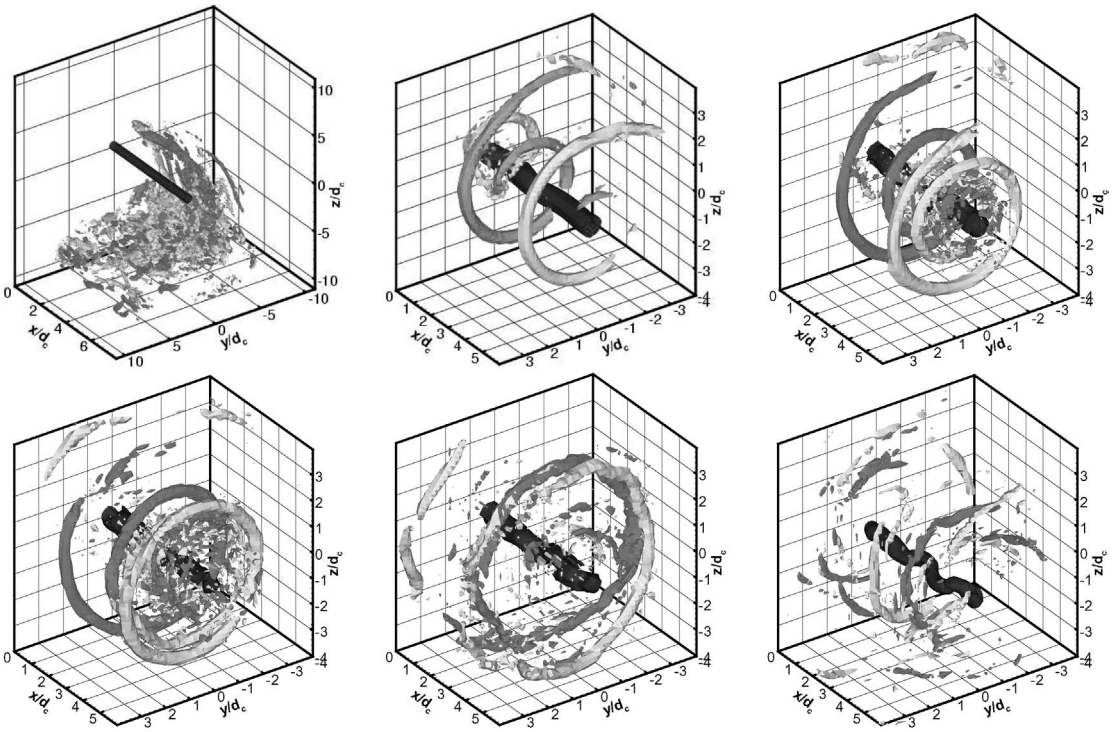

Fig. 6. Vorticity isosurfaces at $d/b = 5.5, 6.5, 7, 7.5, 8.5, 11.5$ (from left to right and top to bottom). Black surface denotes axial component ($\omega_x^* = 3$), azimuthal components ($\omega_\theta^* = 1(-1)$) are plotted in dark (light) grey (from [22]).

The numerical and experimental tangential velocity profiles are shown in Fig. 4(b), at the two locations $d/b = 0.5$ and $d/b = 8$. The half-circle has been added to show the initial position of the jet (the distance between the jet and the vortex centers is equal to $14r_c$ and corresponds to that measured in the experiment at 0.5 wingspan downstream, see also Fig. 5). A quite good agreement between experimental and numerical profiles is observed in the potential region of the vortex. Fig. 6 shows axial and azimuthal vorticity contours in a perspective view at different locations in the wake. At $d/b = 5.5$ the fully turbulent jet is deflected and entrained by the vortex-induced velocity field and starts to wrap around the primary vortex. During that process the jet vorticity is progressively stretched and rearranges to coherent – but spiral-shaped – secondary vorticity structures (SVS) of opposite signs ($d/b = 6.5$). The formation of this structures can be explained by looking at azimuthal vorticity equation, in its incompressible form [60]:

$$\frac{D\omega_\theta}{Dt} = \omega_r \frac{\partial v_\theta}{\partial r} + \frac{\omega_\theta}{r}\frac{\partial v_\theta}{\partial \theta} + \omega_z \frac{\partial v_\theta}{\partial z} \tag{7}$$

where $D(\cdot)/Dt$ is the total derivative. At the beginning of the entrainment phase radial and tangential vorticity components are zero around the core, $\omega_r = \omega_\theta \simeq 0$. However, as the jet is wrapped around the vortex, it induces axial variation to the velocity field, leading to $\partial\omega_\theta/\partial t \simeq \omega_z \partial v_\theta/\partial z \neq 0$. These contra-rotative vorticity structures successively interact, merge and finally decay leading to the relaminarization of the flow at $d/b = 11.5$.

The experimental cross sections of the dimensionless temperature at $d/b = 0.5$ and $d/b = 8$ are presented in Fig. 7. At this stage, the temperature variations are sufficiently weak, corresponding to less than 10% (see Brunet et al. [59]). Consequently, the temperature behaves as a passive scalar. The corresponding numerical results are also displayed in Fig. 7 where averages along the periodic direction x have been performed. The entrainment process shows a stretching and distortion of the interface between jet and external flow, followed by a relatively large-scale engulfment into the rotational region. Furthermore, the comparison shown in Fig. 7 shows that the qualitative features of the jet entrainment are relatively well predicted by the

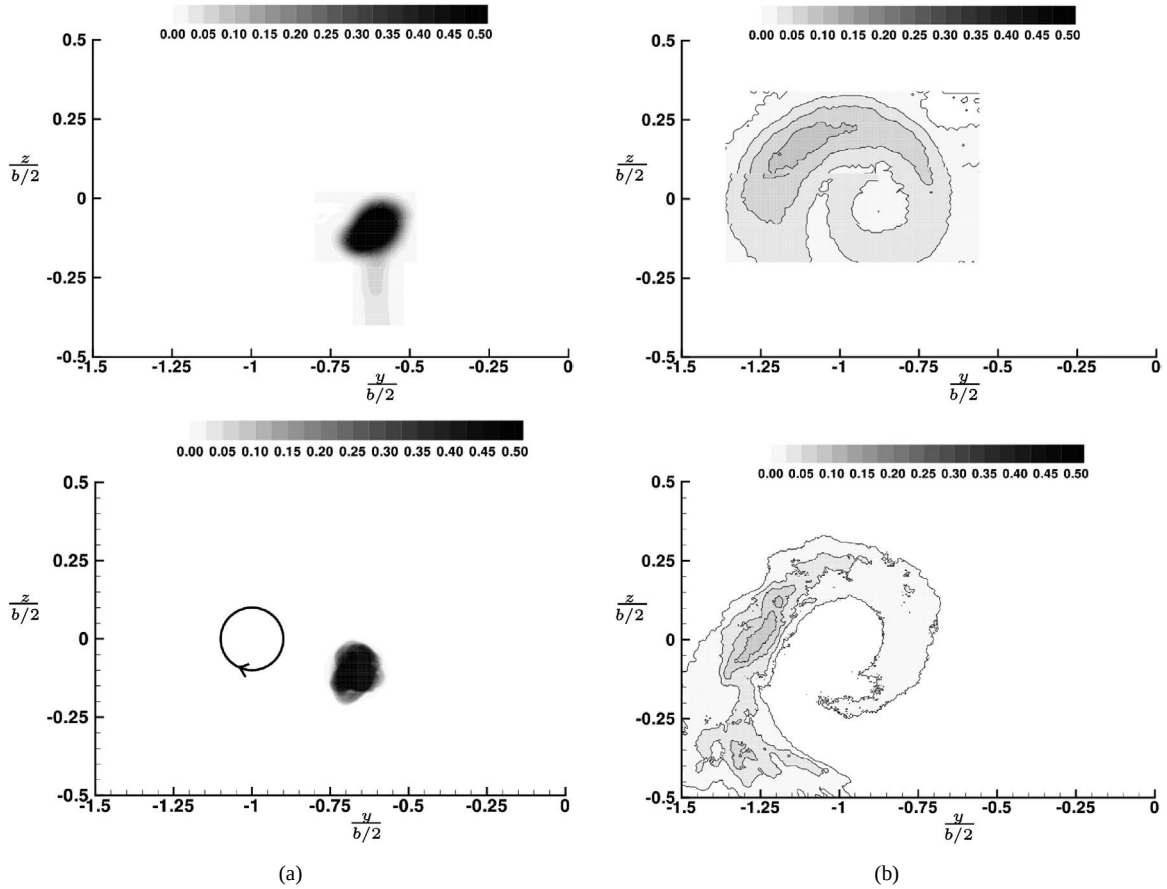

Fig. 7. Comparison between downstream cross-section of the experimental normalized temperature tracer (top) and downstream average of the computational passive scalar (bottom): (a) $d/b = 0.5$; (b) $d/b = 8$ (from [52]).

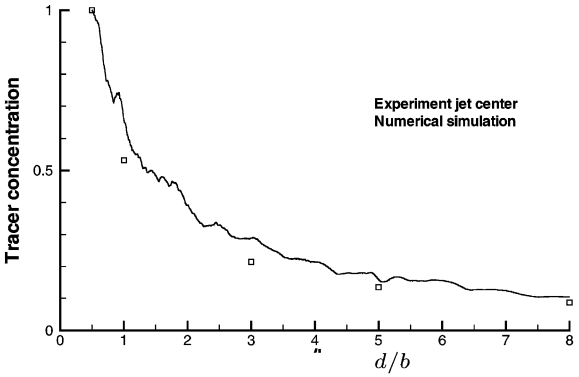

Fig. 8. Comparison between the numerical and experimental downstream evolution of the maximum mixture fraction ('tracer concentration', from [52]).

numerical simulation at 8 wingspans. Nonetheless, the entrainment of the computed jet flow by tangential momentum is slightly delayed. Finally, Fig. 8 presents the downstream variations of the peak values of the experimental normalized temperature and the computed scalar, respectively (both called tracer concentrations). The numerical results show a good agreement with thermocouple measurements, which are comprised inside a 0.5 K error bar (see Brunet et al. [59]), thus providing a good estimation of the downstream evolution of a generic mixture variable.

2.2. High Reynolds large-eddy simulations

The goal of this section is to show the potentiality of LES to reproduce the dynamics and mixing of jet/vortex interaction in the near field wake of an aircraft. In the LES approach equations are filtered spatially, so that any variable $\phi(x)$ may be decomposed into a resolved (or large scale) part $\overline{\phi(x)}$ and a non-resolved (or subgrid-scale) part $\phi''(x)$, with $\phi(x) = \overline{\phi(x)} + \phi''(x)$. This procedure may be obtained by a convolution integral of the variable with a filter function depending on a filter width Δ (which in practice coincides with the mesh cell size). For compressible flows, Favre-filtered variables, defined as $\phi(x) = \tilde{\phi}(x) + \phi'(x)$, with $\tilde{\phi} = \overline{\rho\phi}/\bar{\rho}$ are used. The dimensionless Favre-filtered equations are:

$$\frac{\partial \bar{\rho}}{\partial t} + \frac{\partial(\bar{\rho}\tilde{u}_j)}{\partial x_j} = 0 \tag{8}$$

$$\frac{\partial(\bar{\rho}\tilde{u}_i)}{\partial t} + \frac{\partial(\bar{\rho}\tilde{u}_i\tilde{u}_j)}{\partial x_j} + \frac{\partial \bar{p}}{\partial x_i} = \frac{1}{Re}\frac{\partial \tilde{\tau}_{ij}}{\partial x_j} + \frac{\partial \sigma_{ij}}{\partial x_j} \tag{9}$$

$$\frac{\partial(\bar{\rho}\tilde{E})}{\partial t} + \frac{\partial[(\bar{\rho}\tilde{E} + \bar{p})\tilde{u}_j]}{\partial x_j} = \frac{1}{Re}\frac{\partial \tilde{\tau}_{ij}\tilde{u}_i}{\partial x_j} + \frac{\partial \sigma_{ij}\tilde{u}_i}{\partial x_j} - \frac{1}{RePr}C_p\frac{\partial \tilde{q}_j}{\partial x_j} - \frac{\partial Q_j}{\partial x_j} \tag{10}$$

where the subgrid-scale (SGS) stress tensor $\sigma_{ij} = -(\overline{\rho u_i u_j} - \bar{\rho}\tilde{u}_i\tilde{u}_j)$, and the SGS heat flux $Q_j = \overline{\rho C_p T u_j} - \bar{\rho}C_p\tilde{T}\tilde{u}_j$ are to be modeled, and where the following classical approximations (see Erlebacher et al. [61]) have been made:

- the Favre-filtered shear stress tensor is identified with the filtered shear stress tensor;
- the Favre-filtered heat flux is identified with the filtered heat flux,
- the filtered kinetic energy term $\overline{\rho K u_j}$ in the energy equation is approximated by $\bar{\rho}\tilde{K}\tilde{u}_j - \sigma_{ij}\tilde{u}_j$, where $K = 1/2\,u_i u_i$ is the kinetic energy.

The Favre-filtered passive scalar equation is:

$$\frac{\partial(\bar{\rho}\tilde{Y})}{\partial t} + \frac{\partial(\bar{\rho}\tilde{Y}\tilde{u}_j)}{\partial x_j} = \frac{1}{ReSc}\frac{\partial}{\partial x_j}\left(\mu\frac{\partial \tilde{Y}}{\partial x_j}\right) + \frac{\partial \xi_j}{\partial x_j} \tag{11}$$

The SGS momentum, σ_{ij}, the SGS heat flux, Q_j, and the SGS scalar flux, ξ_j, are modeled through sub-grid scale eddy-viscosity concept:

$$\sigma_{ij} - \frac{1}{3}\sigma_{kk}\delta_{ij} = -2\mu_{\text{sgs}}\left(\tilde{S}_{ij} - \frac{1}{3}\delta_{ij}\tilde{S}_{kk}\right), \qquad Q_j = -\frac{\mu_{\text{sgs}}C_p}{Pr_t}\frac{\partial \Theta}{\partial x_j}, \qquad \xi_j = -\frac{\mu_{\text{sgs}}}{Sc_t}\frac{\partial \tilde{Y}}{\partial x_j} \tag{12}$$

where μ_{sgs} is the SGS dynamic viscosity, $\tilde{S}_{ij}$ is the large-scale strain rate tensor and Sc_t is the turbulent Schmidt number; Pr_t is the turbulent Prandtl number, defining the modified temperature $\Theta = \tilde{T} - (1/(2\bar{\rho}C_v)\sigma_{kk})$, where C_v is the specific heat at constant volume. The values of Sc_t and Pr_t have been set to $Pr_t = Sc_t = 0.3$ which is a good approximation for shear layers, according to Moin et al. [62]. The SGS viscosity model is based on the Filtered Structure Function model of Ducros et al. [63], originally developed by Métais and Lesieur [64] in spectral space and then transposed into physical space. This model insures that the SGS viscosity vanishes when there is no energy at the cutoff wavelength, which is important for the simulation of transitional flows. In particular, recent LES of the elliptical stability of a vortex pair [43] have shown that the model predicts the correct evolution of the core radius during its transition to turbulence, at high Reynolds number $Re = 5 \times 10^5$.

In the present computations, the Reynolds number based on the jet is $Re_j = u_j r_j/\nu = 3 \times 10^6$. Two types of interactions are analyzed: in the first one, referred to as the 'entrainment case', the jet and the vortex initially well separated and the two phases are resolved sequentially, as in the previous section. This configuration is suitable for cruise flight, or for particular high-lift configurations of two-engine aircrafts. The second, referred as the 'blowing case', the jet blows inside the vortex core and is suitable to model high-lift configurations.

2.2.1. *Entrainment case*

During the jet regime, the computational domain has dimensions $L_x = 6r_j$ and $L_y = L_z = 16r_j$ and consists of an equispaced mesh of $61 \times 161 \times 161$ nodes. During the interaction regime, the transversal domain is $L_y = L_z = 30r_j$ and has 301×301, see Fig. 9(a). The grid spacing is then $\Delta_x = \Delta_y = \Delta_z = 0.1\,r_j$ (for the sake of validation a finer grid was also used in the transversal plane with $\Delta_y = \Delta_z = 0.075r_j$, see [53] for details). The core radius and velocity are related to those of the jet by $r_c = r_j$ and $v_c = 1/1.5u_j$, respectively. In the following all results are non-dimensionalized by the turnover time $t_{\text{eddy}} = 2\pi r_c/v_c$, i.e. $t_v = t/t_{\text{eddy}}$.

The Reynolds number LES confirm the qualitative features of the jet/vortex interaction obtained by the DNS of the previous section. The jet instability and transition during the jet regime are well recovered, as confirmed by the evolution of the emerging of the most amplified mode (see [53] for details). The vorticity isocontours of Fig. 10 also show the development of the Kelvin–Helmotz instability during the jet regime. As discussed in the previous section, during the interaction regime the jet is entrained into the vortex field. This is shown in Fig. 11 by the evolution of the isosurface of the vorticity magnitude corresponding to a level $\omega = \omega_{\max}/e^{\beta}$, $\omega_{\max}$ being the actual maximum vorticity (the value which identifies the core of an undeformed Lamb–Oseen vortex). In particular, Fig. 11(a) shows the emergency of three-dimensional structures of azimuthal vorticity ('rings') around the vortex, induced by the jet axial velocity; these structures then progressively decay. As the jet remains outside the core, no strong perturbations are injected in the inner region of the vortex, that may cause its instability. Indeed, Fig. 11(b) shows that the solid body-type rotation of the vortex (see Eq. (6)) prevents the passive scalar from penetrating inside through radial velocity fluctuations.

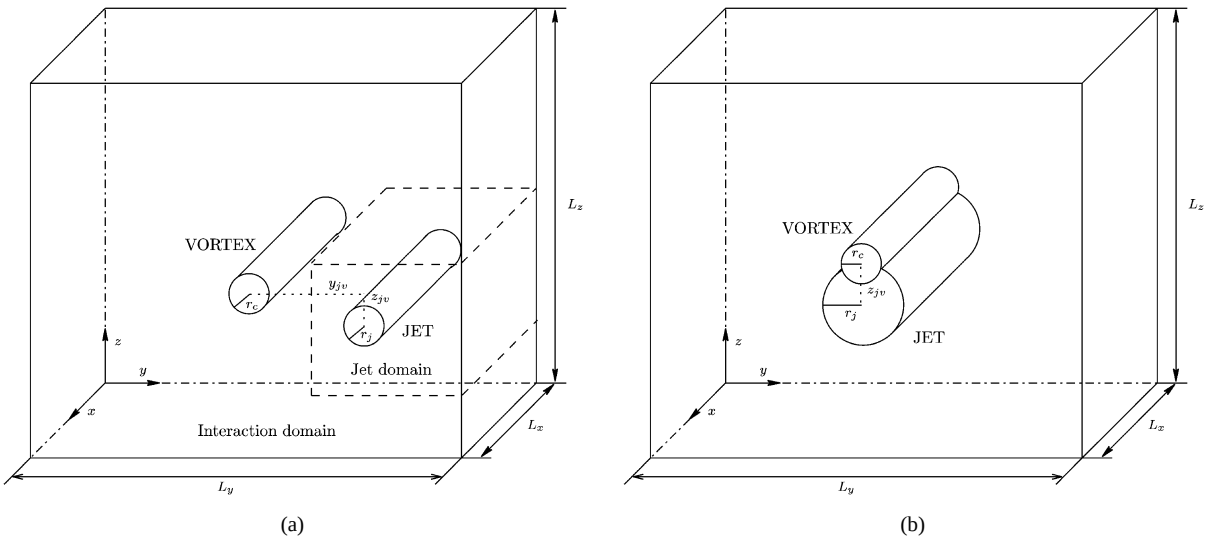

Fig. 9. Computational domains for LES of the jet/vortex interaction: (a) entrainment case; (b) blowing case (from [53]).

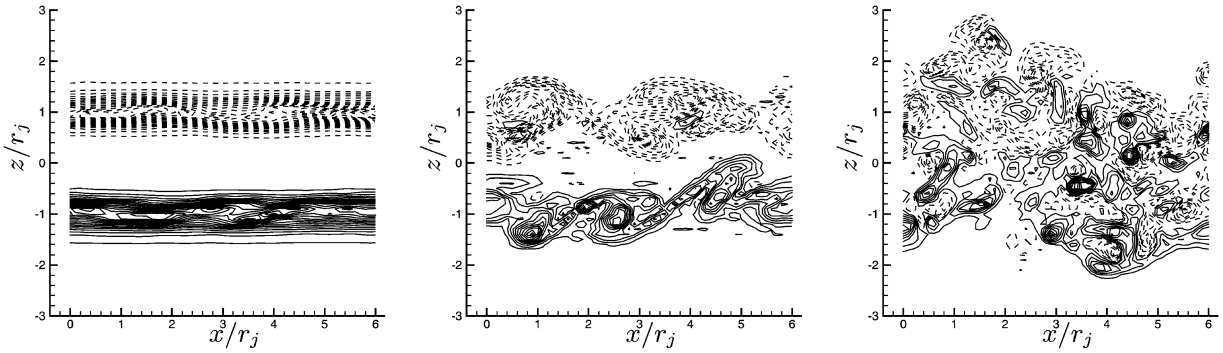

Fig. 10. Evolution of nondimensional azimuthal vorticity ω_y^*: from left to right: $\omega_y^* \in [-2.4; 2.4]$; $\omega_y^* \in [-5.5; 5.5]$; $\omega_y^* \in [-6.0; 6.0]$ (32 levels, solid/dashed lines indicate positive/negative vorticity, from [53]).

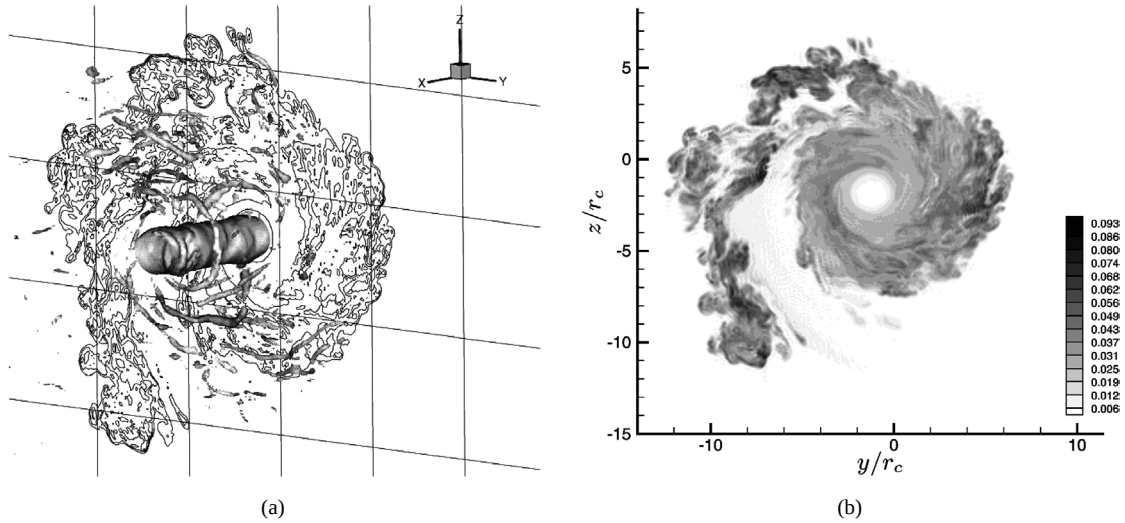

(a) (b)

Fig. 11. Evolution of the vorticity magnitude ω and passive scalar Y, during the interaction phase at $t_v = 17$: (a) a selected vorticity isosurface, $\omega = \omega_{\max}/e^{\beta}$, with superimposed passive scalar plane cut; (b) detailed isocontour lines of passive scalar field at $x = 0$ (from [53]).

2.2.2. *Blowing case*

The computational box consists of $301 \times 301 \times 61$ nodes with $L_x = L_y = 30r_c$, $L_z = 6r_c$, where r_c is the vortex core radius (taken as reference length) while $r_j = 2r_c$ is the jet radius. The origin is taken at the vortex center, the jet and vortex axes are slightly displaced in the vertical direction, $y_{jv} = 0$, $z_{jv} = -2r_c$ (see Fig. 9(b)). Top-hat (Eq. (5)) and Lamb–Oseen (Eq. (6)) profiles are used to initialize the axial velocity $u(r)$ and passive scalar $Y(r)$, and tangential velocity $v_\theta(r)$, respectively. Time is non-dimensionalized by the eddy turnover time t_{eddy} as above, however, no temporal splitting is adopted because the jet and the vortex are close enough for the interaction to start immediately. Indeed, the jet rapidly wraps around the vortex making this flow similar to a swirling jet or a q-vortex [35]. A q-vortex is composed by a Lamb–Oseen vortex and a Gaussian axial flow:

$$v_\theta(r) = \sqrt{\beta}\,\alpha\, v_c \frac{a_c}{r}\left(1 - \exp(-r^2/{a_c}^2)\right) \tag{13}$$

$$u(r) = u_j \exp(-r^2/{a_c}^2) \tag{14}$$

where the dispersion radius $a_c = 1/\sqrt{\beta} r_c = 1/1.12 r_c$ (see Jacquin et al. [49]) is used instead of core radius r_c. Such a flow is usually studied [36,37] by introducing the swirl parameter q, relating peak axial (u_j) and tangential (v_c) velocities,

$$q = \sqrt{\beta}\,\alpha \frac{v_c}{u_j} \simeq 1.57 \frac{v_c}{u_j} \tag{15}$$

An equivalent definition can be devised, based on circulation $\Gamma(r)$ and integral axial momentum $U(r)$:

$$\Gamma(r) = \int_0^{2\pi}\int_0^{r} \omega_z(\zeta)\zeta \,\mathrm{d}\zeta \,\mathrm{d}\theta = 2\pi\alpha v_c r_c\left(1-\exp(-r^2/a_c^2)\right) \tag{16}$$

$$U(r) = \int_0^{2\pi}\int_0^{r} w(\zeta)\zeta \,\mathrm{d}\zeta \,\mathrm{d}\theta = 2\pi u_j \frac{a_c^2}{2}\left(1-\exp(-r^2/a_c^2)\right) \tag{17}$$

where $\omega_z(r) = (1/r(\mathrm{d}rv_\theta)/\mathrm{d}r$ is the axial vorticity. Using Eqs. (15)–(17) leads to $\Gamma(r)/U(r) = 2q/a_c = const$. In a q-vortex, the swirl can be deduced from Γ and W at any radial distance r. In particular, in the limit $r \to \infty$, one has:

$$q = \frac{a_c}{2}\frac{\Gamma(r)}{U(r)} = \frac{a_c}{2}\frac{\overline{\Gamma}}{\overline{U}} \tag{18}$$

where $\overline{\Gamma} = \lim_{r\to\infty}\Gamma(r)$ and $\overline{U} = \lim_{r\to\infty}U(r)$ are the total circulation and integral axial momentum, respectively. Eq. (18) is well adapted to define the swirl in regions of more complex axial flow, as in the present case, where the jet and the vortex are not exactly concentric and the radii are different. Indeed, it is still meaningful if r is taken sufficiently large to account for most of the circulation and the axial momentum affecting the blowing jet region (in practice we take $r = 2r_c$, see Fig. 15(b)).

Two values of the ratio u_j/v_c have been considered here, $u_j/v_c = 1.5$ and 3. Using Eq. (18) with $r = 2r_c$ gives, respectively, $q \simeq 0.5$ and $q \simeq 0.25$, below the stability limit $q = 1.5$ found by Mayer and Powell [36]. Previous numerical simulations of a Batchelor vortex performed by the same authors [51,53] have shown that q increases in the linear stability region and reaches a value of approximately 1.5, corresponding to the saturation of the instability (see Fig. 12(a)); indeed, the tangential velocity does not vary, while axial momentum decreases, and a relaminarization of the flow is reached at later times [37]. As discussed by Jacquin and Pantano [65] this is related to the existence of a 'dispersion buffer', adjacent to the core of a Batchelor vortex. The presence of this buffer zone, whose extent depends on the initial q, prevents perturbations or turbulence generated inside the core from being amplified when reaching the vortex periphery. For high initial swirl, this results in a continuous damping of axial flow, leading to an increase of q and the stability of the flow. However, for low swirl, it is argued in [65] that turbulence may succeed in breaking the stability by transporting angular momentum outside the core, as in the experiments of Kantha et al. [15] or Phillips and Graham [16] (case A, where $q \simeq 0.4$), as well as in the present blowing jet simulations (indeed, for both values $u_j/v_c = 1.5$ and 3, q slightly increases up to $t_v = 1$ and then rapidly decays, see Fig. 12(b)).

The evolution of the tangential velocity profiles is reported in Fig. 13. After $t_v = 1$, the interaction with the unstable blowing jet causes a strong deformation of the velocity profiles, by increasing vortex core size and reducing peak velocity (up to 1/2 v_c at $t_v = 4$). Moreover, the radial distribution of circulation $\Gamma(r)$ in Fig. 14 shows the propagation of a high overshoot, which indicates diffusion of angular momentum outside the core, as also observed by Jacquin and Pantano [65]. This behavior can be explained by looking at the flow structure in Fig. 15 which shows a two-dimensional contour field of axial flow w, superimposed to the vorticity iso-surface $\omega = \omega_{\max}/\mathrm{e}^{\beta}$. During the instability process that leads to the transition to turbulence, the jet partly wraps around the vortex and partly penetrates into its core where it injects strong axial perturbations (swirl is low). Such a process is continuously fed by the (still energetic) axial flow present in the periphery of the vortex, which has indeed the role of an energy reservoir for the whole instability mechanism (as also shown by the evolution of axial velocity profiles in Fig. 13(b)).

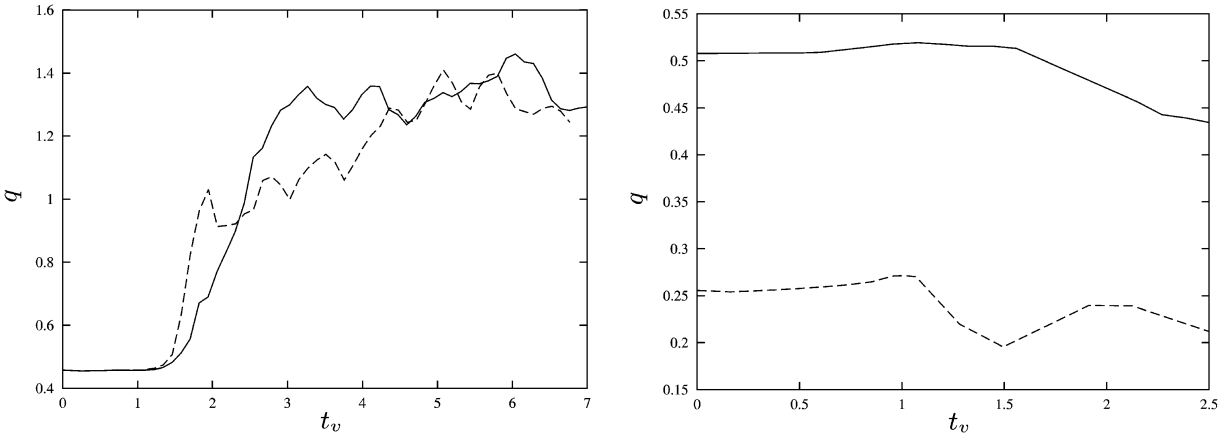

Fig. 12. Time history of the swirl parameter q: (a) Batchelor vortex (from [51]); (b) blowing jet (from [53]).

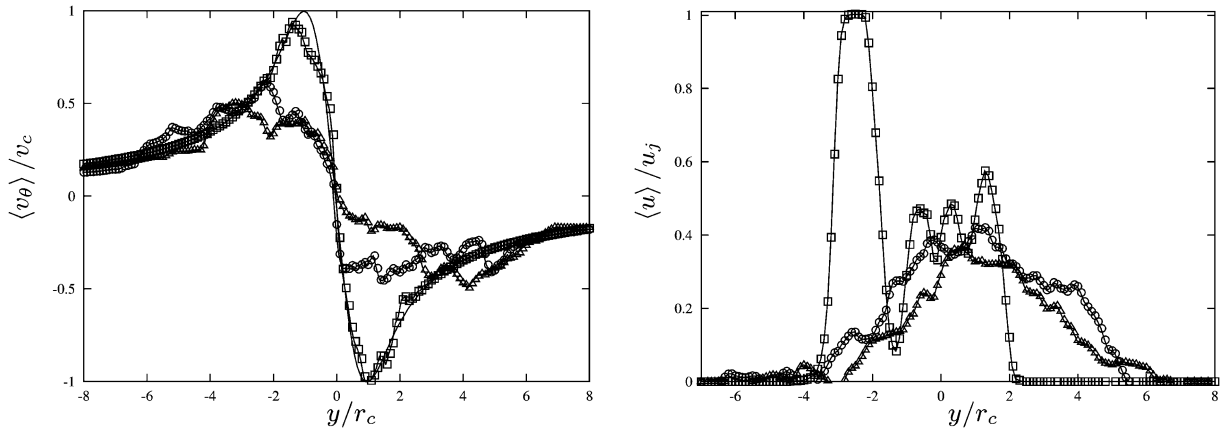

(a) (b)

Fig. 13. Evolutions of the (a) axial-averaged tangential and (b) axial velocity profiles (taken along a line passing through the vortex center): no symbols, $t_v = 0$; □, $t_v = 1$; ○, $t_v = 3$; △, $t_v = 4$ (from [53]).

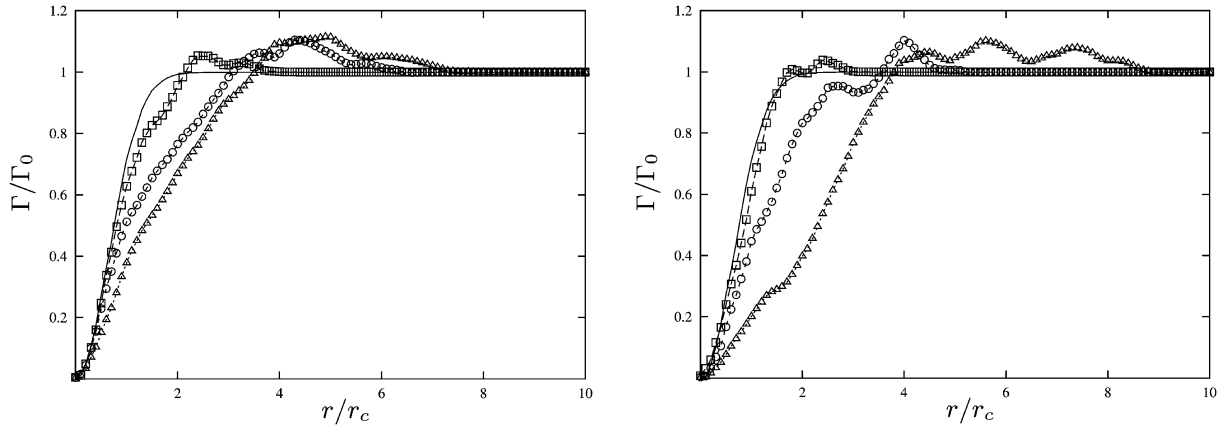

(a) (b)

Fig. 14. Evolution of the radial circulation $\Gamma(r)$ for the case (a) $u_j/v_c = 1.5$ and (b) $u_j/v_c = 3$: no symbols, $t_v = 0$; □, $t_v = 1$; ○, $t_v = 3$; △, $t_v = 4$ (from [53]).

This instability, combined with the low swirl, is responsible for the strong decay of angular momentum, diffusion of the core and deformation of the vortex structure. Indeed, the iso-surface of the λ_2 invariant (see Jeong and Hussain [66]) of Fig. 16 shows that, for the case $u_j/v_c = 3$, at $t_v = 4$, the large-scale vortex coherence is lost, whereas the total circulation remains constant far from the core. Note the difference with a Batchelor vortex where all axial flow is concentrated in the core, axial momentum rapidly decays, leaving the vortex core almost unaffected [51,37].

We conclude this section looking at global mixing. Fig. 17 shows the evolutions of plume areas A_p for both the entrainment and blowing cases. It is defined as the area where the local mixedness function (see Cetegen et al. [67])

$$Z(y,z) = \frac{1}{L_x}\int_0^{L_z} Y(x,y,y)\big(1 - Y(x,y,z)\big)\,\mathrm{d}x \tag{19}$$

is greater than a minimum value $Z_{\min}$ (here we assumed $Z_{\min} = 0.001$, a different choice of such a threshold only causes a global displacement of the curve but does not affect its slope). The figure shows that A_p remains constant up to the transition and then increases linearly, with slope $\chi_p = \mathrm{d}(A_p/\pi r_j^2)/\mathrm{d}t_v$ that depends on the initial jet/vortex configuration. In particular, in the blowing-jet cases the plume areas are smaller and the jet remains concentrated because of the absence of large-scale vortex entrainment (see [53] for details).

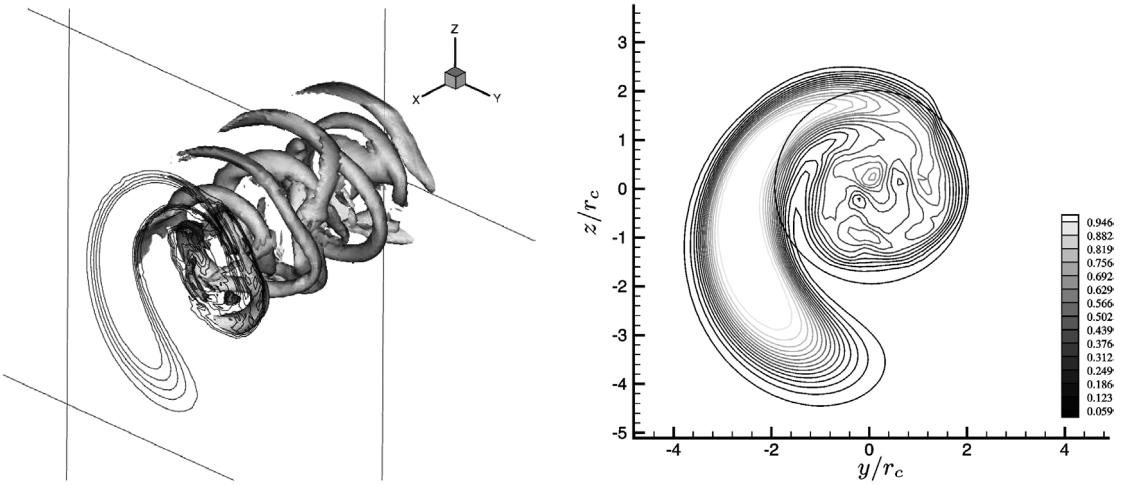

(a) (b)

Fig. 15. Flow structure at $t_v = 1$: (a) iso-surface of the vorticity magnitude ($\omega = \omega_{\max}/e^{\beta}$) and passive scalar plane cut (5 levels from 0 to 1); (b) two-dimensional axial-averaged contour field of axial velocity (the blowing jet region, $-2r_c < r < 2r_c$, is identified by dashed lines, from [53]).

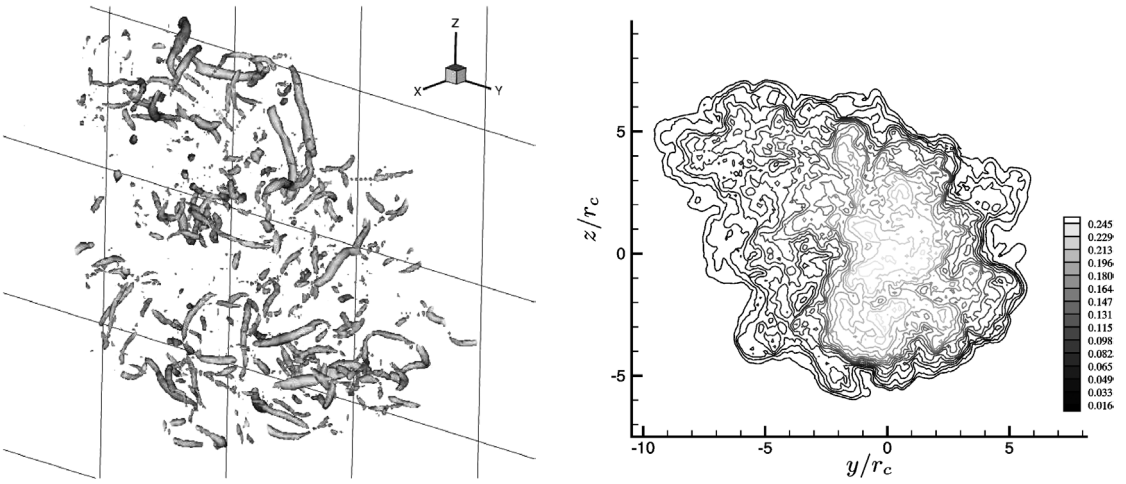

(a) (b)

Fig. 16. Flow structure at $t_v = 4$ ($w_j/v_c = 3$): (a) iso-surface of λ_2 invariant [66]; (b) two-dimensional axial-averaged passive scalar contour field (from [53]).

3. Environmental applications

Aircraft exhaust contains gases resulting from combustion, usually designated as major species (CO_2, CO, H_2O, NO_x), associated with a number of minor effluents, in a gaseous or solid phase, including OH, carbon particles, unburnt hydrocarbons and sulphur species. These species can lead not only to homogeneous chemical transformations but also to ice nucleation and growth processes that will form contrails in the atmosphere or to sulphuric bimolecular nucleation that will increase the local aerosol burden. This last process has an impact on the cloudiness and may have an impact on the consequent radiative budget, but it can also modify the chemical transformations through heterogeneous processes. Furthermore, adsorption of the species by liquid water or ice particles can lead to elimination of some of the soluble species by sedimentation, followed by re-evaporation or definitive deposition through local precipitation. Two environmental applications of the jet/vortex interaction are discussed in detail in the next sections.

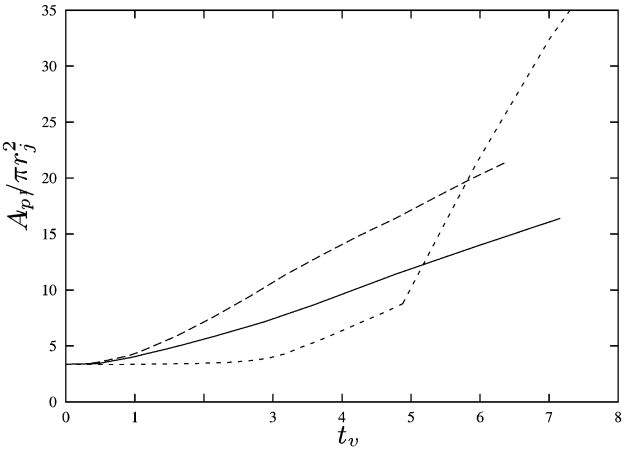

Fig. 17. Temporal evolutions of plume areas $A_p/\pi r_j^2$: solid line, blowing case, $w_j/v_c = 1.5$; dashed line, blowing case, $w_j/v_c = 3$; dotted line, entrainment case (from [53]).

3.1. Gas-phase chemistry: NO_x conversions

The objective of this section, which constitutes a part of a work described in detail in Garnier et al. [6], is the investigation of the potential transformation of the active species emitted from aircraft into reservoir species. The analysis is based on modeling the chemical transformations in the near-field region, up to one kilometre behind a Boeing 767 equipped with 2 RB211 engines, flying at mid-altitude at noon. The potential chemical transformations of important species such as NO, NO_2, HNO_2, HNO_3 and H_2SO_4 are considered. Chemistry is calculated using a box model including the photochemical and heterogeneous reactions. The basic objective of the present section is to explore the relative importance of the various parameters involved in the NO_x transformation in the near field of an aircraft wake. The investigation is mainly oriented towards the HNO_3 and HNO_2 creation from NO_x because they are expected to be the main NO_y species in the range of altitude of subsonic aircraft, and they can potentially be eliminated through dissolution in water, or be captured by the ice crystal surface and transferred at different location or altitude. In the present study, the analysis has been limited to the near field: investigation of the hot jet and the first kilometer behind the engine in the cold conditions created by the vortex.

The important chemical families in the plume are NO_y (including NO, NO_2, HNO_3, HNO_2 and N_2O_5), HO_x (including OH and HO_2), SO_x (including SO_2, SO_3 and H_2SO_4) and CH_x (including CH_4 and CH_2O), NMHC has been ignored. The chemical modeling is supported by a photochemical box model including kinetic constants and absorption cross sections generally compiled from De More et al. [68]. Chlorine and bromine reactions have been omitted, due to their limited amount at 10 km at midlatitudes. To start with, the heterogeneous reactions any potential reaction between gas and aqueous phase involving the liquid transition between solid and gas has been ignored at this state. Only one heterogeneous reaction on ice has been included:

$$N_2O_5 + H_2O_{ice} \rightarrow 2HNO_3 \tag{20}$$

The reaction probability for this reaction is calculated by the classical formulation $k(s^{-1}) = 1/4v\gamma IEA$ where γ is the reaction probability (see e.g. [69,70]), v is the mean velocity of molecules and *IEA* is the ice equivalent surface area per cubic centimetre. The formation of N_2O_5 is mainly due to the $NO_3 + NO_2$ reaction. Although NO_3 is mainly formed at night, the diurnal variation of N_2O_5 is weak. The reaction scheme for the formation of gaseous H_2SO_4 has been proposed by Stockwell and Calvert [71] and re-investigated by Arnold et al. [72] and Reiner and Arnold [73], and more recently by Starik et al. [74,75] and Sorokin et al. [76]:

$$SO_2 + OH + M \rightarrow HSO_3 + M \tag{21}$$

$$HSO_3 + O_2 \rightarrow SO_3 + HO_2 \tag{22}$$

$$SO_3 + H_2O + M \rightarrow H_2SO_4 + M \tag{23}$$

(note that the kinetic constant for the last reaction is 2.4×10^{-15} mol^{-1} cm^3 s^{-1} which corresponds to the upper limit deduced from the experiment of [73]).

A parametric study has been made to evaluate the importance of the OH mixing ratio on the potential creation of HNO_3, HNO_2, and H_2SO_4 inside the jet flow. The box model has been run using several values of OH mixing ratios and temperature, for noon conditions, and for a limited period of time corresponding to the hot jet phase (0.1 s). The time evolution of the

active species was simulated for two constant temperatures 560 K, the maximum value in the jet, and 220 K, the background atmospheric temperature with initial OH conditions 10^{-9} and 10^{-5}. The results show that the reaction leading to HNO_2 and HNO_3 production is directly driven by OH at the nozzle exit, and for high OH mixing ratio, HNO_2 and HNO_3 can reach several ppm. In the extreme case at the nozzle exit, where the maximum value for OH, 10^{-5} and the highest temperature, 560 K are attained, 6% of the NO_x concentration is converted into HNO_2 and HNO_3 (respectively 4.5% and 1.5%). The same sensitivity appears for the H_2SO_4 value which levels are highly dependent on OH at the beginning of the jet but not very sensitive to the temperature. The final N_2O_5 is also affected by the initial OH mixing ratio, but is more affected by the temperature. The final OH value remains below 1 ppt in both temperature conditions i.e. not far from the background and far away from the initial OH emission. These low levels could indicate that there is precedence for OH starvation, inside the jet flow. This is important, because, in any case, the high OH emission level will not cause high reactivity along the following part of the wake. Finally, the most relevant species for the chemistry in the wake, such as OH, N_2O_5, HNO_3, H_2SO_4, HNO_2, are affected by large uncertainties depending on the OH emission rate, however, these uncertainties do not appreciably affect the total NO_x.

The fluid-chemistry coupling is obtained by solving the chemical reaction equations at each computational time step along different trajectories chosen throughout the vortex wake. Chemical species are treated separately and convected following the converged solution. In this case the chemical transformations of species are assumed to have no effect on the dynamics of the fluid flow. The emission indices for CO_2 and H_2O are 3141 g/kg and 1281 g/kg, respectively, and are representative of typical aircraft fuels as used today. The main species concentrations used as initial conditions in model simulations of the wake chemistry are listed in the second column of the Table 1 which shows the evolution, for noon conditions, of some species along a trajectory from the exhaust exit up to 1000 m. This evolution depends on the reactivity of the species and on the background composition of the atmosphere. Some species, chemically inert (like CO_2 and H_2O), illustrate the evolution of the dilution rate, up to the time they become close to the background. The differences in CO_2 and H_2O reaching background levels are only due to differences in the background level while, beyond 1000 m, NO is still 4 orders of magnitude above the background level. If the chemical evolution of NO were negligible one could observe that the dilution factor D_{NO} between the two extremes varies by a factor of 500. This computed value is in the range of the dilution factor values measured inside the plumes of several aircrafts (see Schumann et al. [5]). When the species exist only in the background and are supposed negligible inside the jet flow, no evolution appears because the dilution factor, at the beginning of the interaction phase being about 0.26 (at 29 m behind the engine), does not seriously affect the natural atmosphere (see for example CH_2O). The mixing ratio for NO and NO_2 at 2 km measured behind a DC9 (see Arnold et al. [72]) is a factor of 4 higher than that calculated at only 1 km behind a Boeing 767. The measured NO/NO_2 ratio is close to 0.25 while the calculated one is 0.1. The measured HNO_3/HNO_2 ratio is 1.1 while that calculated is 0.45. The main reason for this discrepancy probably comes from the different parameters used in calculations

Table 1
B-767 aircraft. Mixing ratios of chemical species resulting from the simulation along a typical air stream for noon conditions

Species	Exit emissions	29 m	100 m	500 m	1000 m	Background
NO	6.6×10^{-5}	$*1.32 \times 10^{-5}$	3.5×10^{-6}	2.5×10^{-7}	3.55×10^{-8}	6.0×10^{-12}
NO_2	6.6×10^{-6}	$*1.3 \times 10^{-6}$	3.0×10^{-7}	2.5×10^{-8}	3.65×10^{-9}	2.0×10^{-12}
NO_x	7.2×10^{-5}	$*1.45 \times 10^{-5}$	3.3×10^{-6}	2.75×10^{-7}	3.91×10^{-8}	8.0×10^{-12}
HNO_3	0.0	$*2.4 \times 10^{-7}$	4.0×10^{-8}	3.0×10^{-9}	8.41×10^{-10}	3.0×10^{-10}
HNO_2	0.0	$*6.2 \times 10^{-7}$	5.0×10^{-8}	5.0×10^{-9}	2.3×10^{-9}	7.0×10^{-11}
N_2O_5	0.0	$*1.0 \times 10^{-11}$	3.0×10^{-12}	7.0×10^{-13}	6.0×10^{-13}	6.0×10^{-13}
HO_2NO_2	0.0	9.6×10^{-12}	1.0×10^{-11}	1.0×10^{-11}	1.2×10^{-11}	1.2×10^{-11}
OH	1.0×10^{-5}	$*2.0 \times 10^{-13}$	1.1×10^{-14}	2.1×10^{-13}	5.4×10^{-13}	6.0×10^{-14}
HO_2	0.0	4.8×10^{-12}	1.1×10^{-13}	2.1×10^{-13}	6.0×10^{-13}	6.0×10^{-12}
H_2O(g)	3.5×10^{-2}	$*7.0 \times 10^{-3}$	1.2×10^{-3}	1.2×10^{-4}	5.5×10^{-5}	3.6×10^{-5}
O_3	0.0	3.2×10^{-8}	4.0×10^{-8}	4.0×10^{-8}	4.0×10^{-8}	4.0×10^{-8}
SO_2	6.6×10^{-6}	$*1.32 \times 10^{-6}$	2.6×10^{-7}	2.6×10^{-8}	3.65×10^{-9}	1.0×10^{-10}
H_2SO_4(g)	0.0	$*4.2 \times 10^{-8}$	6.0×10^{-9}	4.0×10^{-10}	8.9×10^{-11}	1.1×10^{-12}
SO_3	0.0	0.0	2.0×10^{-13}	7.0×10^{-13}	7.0×10^{-13}	7.0×10^{-13}
CH_4	1.7×10^{-6}	1.3×10^{-6}	1.6×10^{-6}	1.6×10^{-6}	1.6×10^{-6}	1.6×10^{-6}
CH_3O_2	0.0	6.4×10^{-13}	1.0×10^{-15}	3.0×10^{-14}	7.0×10^{-14}	8.0×10^{-13}
CH_2O	0.0	2.0×10^{-11}	2.5×10^{-11}	2.5×10^{-11}	2.5×10^{-11}	2.5×10^{-11}
CO	2.96×10^{-5}	$*6.0 \times 10^{-6}$	2.0×10^{-6}	1.1×10^{-7}	7.0×10^{-8}	5.6×10^{-8}
CO_2	3.14×10^{-2}	$*6.3 \times 10^{-3}$	5.0×10^{-4}	4.0×10^{-4}	3.6×10^{-4}	3.5×10^{-4}

* Values deduced from the chemical hot jet calculation. The others concentrations correspond to atmospheric level taking into account the dilution calculated in the vortex wake. Atmospheric conditions at 35000 ft altitude were adopted for the background compositions, $p_{atm} = 24000$ Pa, $T_{tam} = 219$ K (corresponding to the tropopause level), $N_{atm} = 7.9 \times 10^{18}$ mol/cm^3 (from [6]).

such as the type of engine, aircraft, atmosphere. The high level of H_2SO_4 shown in the third column of Table 1, is only produced by the oxidation of SO_2 in the first phase (i.e. the hot jet).

The behaviour of the OH and HO_2 evolution along the jet and the wake is typical of the local concentration of the species and especially of the NO (and SO_2) local level. Just after the exit, due to the very high NO level (about 10^{-5}), OH is completely scavenged to product HO_2 then NO_2, HONO, HNO_3, H_2SO_4. Using a chemical box model to analyse the OH/HO_2 tendency versus the NO concentration it appears that after a very short time of the order of a tenth of second and due to the final reaction:

$$HO_2 + NO \rightarrow NO_2 + OH \tag{24}$$

the residual OH/HO_2 ratio is representative of the local NO level and can reach a level higher than 100 for an NO level around 10^{-7}. Then following the mixing with the atmosphere and the NO slow decrease, OH and HO_2 have a trend to increase, eventually exceeding the background level, while the OH/HO_2 ratio slowly returns to the atmospheric background (typically 0.01). In the example which has been calculated, after 1 km the OH/HO_2 ratio is of the order of 1 while the OH concentration is about 10 times the natural background level. This result is weakly dependent on the photodissociation. However, within higher time scale, the photodissociation mechanisms become more and more important and also lead to perturbations in the OH/HO_2 ratio.

3.2. Contrail formation in aircraft wakes

Contrails are ice clouds which mainly form by condensation of exhaust and ambient water vapor over suitable nucleation sites, such as soot particles and sulfur aerosols, emitted by aircraft engines (see Appleman [77] and Schumann [78]). If the ambient temperature is lower than a threshold value, contrails form when the air surrounding the particles becomes supersaturated with respect to water. This may occur somewhere in the jet plume, as the result of the increased humidity due to mixing between hot and moist exhaust gases with cold and less humid ambient air. If ambient air is also supersaturated with respect to ice, contrails are expected to be persistent (see Schumann [78] for a complete analysis). Formation and persistence of contrails have been studied in atmospheric science literature by means of experiments (see e.g. Petzold et al. [79], Schröder et al. [80] and Schumann et al. [81]) and numerical simulations with different levels of sophistication for the microphysical and radiative models (generally employing 'bulk' formulation for the ice phase). For example, Sussmann and Gierens [82] and Lewellen and Lewellen [83], and Gierens [84] analyzed, respectively, the development and the persistence of contrails and their interaction with the atmosphere up to tens of minutes from the emission time.

The goal of this section is to present a computational methodology, developed by Paoli et al. [85], to simulate the early evolution of a contrail in the near-field wake, i.e. up to a few seconds from the emission time. To that end, a two-phase flow approach is used, by assuming that the medium consists of a gaseous carrier phase and a solid, dispersed phase (soot particles and ice crystals). Large-eddy simulations have been carried out for the carrier phase using the solver described in Section 2. A Lagrangian particle-tracking method has been used for the dispersed phase to track particle movement (gas variables are evaluated at particle positions using a linear interpolation). Due to their small size (the radius r_p varying from tens of nanometers to a few microns, during the early contrail evolution, see e.g. [86]), the particles relaxation time $\tau_p = 4\rho_p r_p^2/18\mu$ is small (10^{-8} s to 10^{-5} s) compared to the flow characteristic time-scales at the filtered size. Therefore they can be treated as tracers which follow the carrier phase. On the other hand, strong mass exchanges between the ice and vapor phases takes place because of the large particle number density, varying between 10^9 and 10^{11} m^{-3}, a few seconds after the emission. This also implies that only clusters of particles, or 'numerical particles', can be carried, each one containing a large number n_{trans} of real soot-ice kernels (as discussed by Paoli et al. [87]; this approach can be seen as a particular case of the method of moments used to solve a Liouville equation for particles conservation in four-dimensional space (x, y, z, r_p)). A numerical particle is defined as the center of mass, $\underline{x}_p$, of n_{trans} physical particles. In the tracer limit, its motion is completely described by:

$$\frac{\mathrm{d}\underline{x}_p}{\mathrm{d}t} = \underline{\tilde{u}}(\underline{x}_p) \tag{25}$$

where $\underline{\tilde{u}}$ is the (filtered) gas velocity. Using filtered quantities in Eq. (25) is equivalent to neglecting sub-grid dispersion, compared to the resolved, large scale dispersion (due to the high Reynolds number). Gas sources are estimated at the numerical particle positions with the point source approximation, afterwards they are projected on the Eulerian grid, which is equivalent to the application of a spatial filtering (see Yeung and Pope [89] and Boivin et al. [88] for details). Momentum exchange is negligible in the tracer limit; furthermore, temperature cannot be modified by ice growth by more than a few Kelvin (see [78]), so thermal exchanges from particles to gas are also neglected. Hence, only mass exchange are considered by adding a source term ω to Eqs. (8) and (11), with $Y \equiv Y_w$ being the water vapor mass fraction,

$$\frac{\partial \bar{\rho}}{\partial t} + \frac{\partial(\bar{\rho}\tilde{u}_j)}{\partial x_j} = \omega \tag{26}$$

$$\frac{\partial(\bar{\rho}\tilde{Y}_w)}{\partial t} + \frac{\partial(\bar{\rho}\tilde{Y}_w\tilde{u}_j)}{\partial x_j} = \frac{1}{Re\,Sc}\frac{\partial}{\partial x_j}\left(\mu\frac{\partial\tilde{Y}_w}{\partial x_j}\right) + \frac{\partial\xi_j}{\partial x_j} + \omega \tag{27}$$

The term ω is negligible in Eq. (26) because of the small amount (order of few percent) of water vapor in the exhaust gases. On the other hand, in Eq. (27), it accounts for vapor/ice phases exchange using the model proposed by Kärcher et al. [90]. In this model, nucleation processes are not considered. Furthermore, ice is assumed to grow via vapor condensation onto ice nuclei, e.g. soot particles (assumed already activated), by means of a simple diffusion law, proportional to the local ice supersaturation. Note that this assumption oversimplifies the actual microphysics in contrails; in fact, there is now experimental evidence (see e.g. [3]) that condensation mainly starts to form liquid droplets that successively freeze (the pathway corresponding to direct ice nucleation below water saturation being less likely to occur, see Kärcher [91] and Kärcher et al. [92]). Nevertheless, the model contains important physical parameters of the condensational process and represents a first step towards the integration of 'richer' microphysics models into complex two-phase flow LES solvers.

In dimensionless form, the growth rate of a single crystal $\dot{r}_p$ and the rate of change of water vapor mass fraction ω are given by (N_p is the total number of numerical particles and all bars and tildes are removed for simplicity):

$$\dot{r}_p = \frac{G(r_p)(Y_w - Y_{\text{sat}})}{\rho_p r_p Re\,Sc} \tag{28}$$

$$\omega(\underline{x}) = -\sum_{p=1}^{N_p} n_{\text{trans}}\delta(\underline{x} - \underline{x}_p)4\pi r_p^2\rho_p\dot{r}_p \tag{29}$$

where ρ_p is the non-dimensional ice density and Y_{sat} is the vapor mass fraction at saturation (related to the molar fraction, X_{sat}, by $Y_{\text{sat}} = X_{\text{sat}}/(X_{\text{sat}} + (1 - X_{\text{sat}})\,W_{\text{air}}/W_w)$, with $W_{\text{air}} = 28.85$ Kg/Kmole, $W_w = 18.01$ Kg/Kmole), while saturation conditions are estimated by Sonntag [94].

The collisional factor $G(r_p)$ in Eq. (28) is given by a semi-theoretical correlation, $G(r_p) = (1/(1 + Kn) + 40Kn/3)^{-1}$, which accounts for the transition from gas kinetic to the continuum regime and was found to give good results for quasi-isothermal flows and low heat transfer problems see (Qu and Davis [93]). It is parametrized by the Knudsen number, defined as the ratio of the vapor mean free path to the soot-ice kernel radius, $Kn = \lambda/r_p$. The mean free path is evaluated through $\lambda = (\sqrt{2}\pi\,d^2 n_w)^{-1}$ which depends on the vapor molecular cross section $\pi\,d^2$ and number density n_w. Three values of λ were considered by Paoli et al. [85] to check the sensitivity of the ice growth model. The analysis showed that reducing λ increases the growth rate whereas it does not affect the final value of the radius which corresponds to the thermodynamic equilibrium state at the (fixed) saturation conditions.

The basic configuration adopted in this study consists of an exhaust jet, loaded with water vapor and soot particles, interacting with a wing-tip trailing vortex. A two-stage simulation was used, the flow parameters and the computational domain are the same as described in Section 2.2 (see also Fig. 9(a)). Axial velocity, temperature and vapor mass fraction are initialized according to a tanh law,

$$u_0(r) = \frac{1}{2}\big[(u_j + u_a) - (u_j - u_a)F(r)\big], \qquad T_0(r) = \frac{1}{2}\big[(T_j + T_a) - (T_j - T_a)F(r)\big]$$
$$Y_{w_0}(r) = \frac{1}{2}\big[(Y_{w_j} + Y_{w_a}) - (Y_{w_j} - Y_{w_a})F(r)\big] \quad \text{with } F(r) = \tanh\left[\frac{1}{4}\frac{r_j}{\theta}\left(\frac{r}{r_j} - \frac{r_j}{r}\right)\right] \tag{30}$$

In the present study, no coflow is assumed, $u_a = 0$, and the background water content is zero, $Y_{w_a} = 0$. The exhaust water content, taken from available literature data [6], is $Y_{u_j} = 0.03$, while ambient and exhaust temperatures are, respectively, $T_a = 220$ K and 440 K, giving $T_j/T_a = 2$. The jet is loaded with $N_p = 250\,000$ (numerical) soot particles with the same radius $r_p(0) = 0.02$ μm. They behave as tracers and each one represents a packet of $n_{\text{trans}} = 10^6$ physical particles.

A first set of LES was performed with the ice-growth model switched off. The object was to obtain a reference mixing case in high Reynolds conditions typical of aircraft wake configurations. It was also useful to analyze the spatial distribution of supersaturated particles and identify the regions where ice formation is most likely to occur. Basic diagnostic consists in analyzing the thermodynamic properties of the exhaust gas during mixing with ambient air. As shown in [85], the joint Probability Density Function (PDF) of normalized temperature, $(T - T_a)/(T_j - T_a)$, and water vapor partial pressure, $(p_w - p_{w_a})/(p_{w_j} - p_{w_a})$ follows a straight line which indicates pure mixing between hot jet and cold air. This is a consequence of low Mach number and the assumption that turbulent (besides molecular) diffusivities are the same, $Sc_t = Pr_t = 0.3$. The first implies small pressure fluctuations and kinetic energy negligible compared to internal energy. The latter implies the same diffusion terms for T and p_w which are then solved by the same transport equations and evolve along a mixing line

$$\frac{p_w}{p_{w_j} - p_{w_a}} = \frac{T}{T_j - T_a} + \frac{1}{2}\left(\frac{p_{w_j} + p_{w_a}}{p_{w_j} - p_{w_a}} - \frac{T_j + T_a}{T_j - T_a}\right) \tag{31}$$

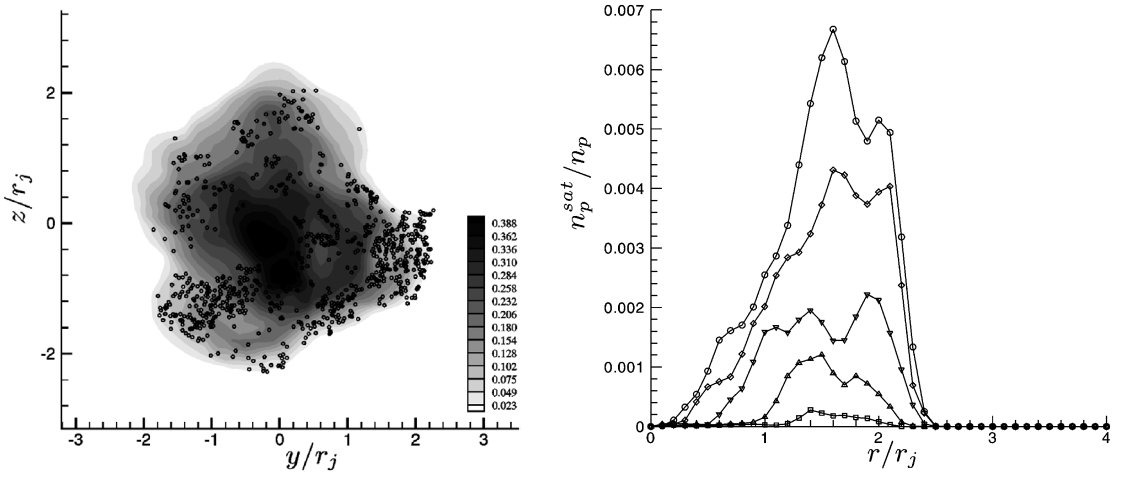

(a) (b)

Fig. 18. Jet phase: (a) plane cut of vapor content Y_w and distribution of supersaturated particles ($t = 0.73$ s); (b) evolution of the radial distribution of supersaturated particles: □, $t = 0.6$ s; △, $t = 0.63$ s; ▽, $t = 0.67$ s; ◇, $t = 0.7$ s; ○, $t = 0.73$ s (from [85]).

(a) (b)

Fig. 19. Particle distribution during the jet/vortex interaction phase: (a) $t = 1$ s; (b) $t = 1.7$ s. Dry soot particles are represented in black, iced supersaturated particles in light grey. The iso-surface of the vorticity magnitude (in green) identifies the vortex and the secondary structures around the vortex core (from [85]).

(obtained by elimination of r in Eq. (30)). All particles are initially placed below the saturation curve p_{sat} because they are still concentrated inside the hot jet region. Due to the mixing with cold air, particles cool, down moving along the mixing line, until some of them become supersaturated (not shown). The spatial distribution of supersaturated particles is provided in Fig. 18(a), together with a plane cut of water vapor content during the jet phase. The figure shows that air first saturates around the particles at the edges of the jet where temperature has dropped and there is sufficient vapor to condense. This is quantified in Fig. 18(b) which shows the number of supersaturated particles as a function of the radial distance from the jet. The large peak at $r = 1.5\,r_j$ identifies the region of maximum accumulation of saturated nucleation sites.

The dynamics during the interaction phase is dominated by the entrainment of the exhaust vapor by the wake vortex (see Fig. 19 and Section 2). This mechanism of entrainment enhances mixing with external air. Exhaust cooling and vapor conden-

sation are favored by the presence of the vortex, as indicated in Fig. 19 which shows that all particles are supersaturated at $t = 1.7$ s, thus indicating that the contrail can form everywhere in the wake.

3.2.1. Growing particles

This section presents the results of the simulations with the ice-growth model activated, Eqs. (28) and (29), with an initial Knudsen $Kn(0) = 2.5$. The goal is to analyze how the contrail forms, grows and influences vapor mixing. Fig. 20(a) displays the temporal evolution of the mean crystal radius, $r_p^{\text{mean}} = \sqrt{\sum_p r_p^2}/N_p$, which is a measure of the average contrail dimensions. Up to $t \simeq 0.7$ s, corresponding to the end of the jet phase, r_p^{mean} does not change with respect to the initial value of dry-particle radius, $r_p(0) = 0.02$ µm. It starts to grow at the beginning of the interaction phase when the high supersaturation $Y_w - Y_{\text{sat}}$ induced by the presence of the wake vortex significantly increases the growth rate $\mathrm{d}r_p/\mathrm{d}t$. Later on, at $t \simeq 2$ s the growth slows down and finally the mean crystals radius reaches a plateau value of $r_p^{\text{mean}} \simeq 4.25$ µm at $t = 3$ s. This is explained by observing that, as long as particles freeze, exhaust vapor is either removed or diluted in the jet plume by large-scale vortex entrainment and turbulent diffusion (see [53]). This reduces the mass fraction Y_w, the local supersaturation and the growth rate $\mathrm{d}r_p/\mathrm{d}t$, as indicated by Eq. (28). Associated to the growth of particles' radius, the total mass of ice $m_{\text{ice}} = \sum_p 4/3\pi r_p^3 \rho_p$ increases, reaching the remarkable value of 60% of the total initial vapor mass content. Such a strong mass exchange by vapor removal affects exhaust dilution properties: in fact, vapor partial pressure p_w decreases at a faster rate than temperature T (the latent heat of condensation is negligible) which causes a significant deviation from the theoretical mixing line, as shown in Fig. 20(b). The figure reports the scatter plot of p_w and T interpolated around each particle at different times during the interaction phase. It also shows that particles enter the supersaturation region in the thermodynamic plane (T, p_w), then move towards and finally collapse onto the saturation curve p_{sat}. This indicates that thermodynamic equilibrium between vapor and ice phases is reached according to the local thermodynamic conditions experienced by each particle during its motion around the wake vortex. A general feature of the jet entrainment process by the vortex is that particles which freeze first attain the larger asymptotic radius, as shown in Fig. 21(a), because they find more vapor available for condensation. In particular, after complete entrainment, larger ice crystals are nearly equi-distributed, as a function of the distance from the vortex (not shown).

The distribution of ice crystals size is provided in Fig. 21(b) in terms of radius PDF. The peak around $r_p(0) = 0.02$ µm at $t = 0.73$ s (end of the jet phase) indicates that only a small amount of ice has formed. As long as ice nucleation proceeds, such a peak decreases and finally disappears, and the shape of the PDF finally approaches a Gaussian at $t = 3$ s. An important result for contrail optical properties is the variance, $var(r_p)/r_p^{\text{mean}} \simeq 0.125$, which indicates polydispersion, whereas temperature and partial pressure around particles has become approximatively uniform.

Fig. 22 finally presents the normalized PDF of water vapor mass fraction Y_w in the overall domain, which identifies the instantaneous state of the available water vapor. Initially the PDF is characterized by a quasi two-delta function at 0 and $Y_w = 0.03$ (not shown). The figure reports the PDF at $t = 1.7$ s, which corresponds to the highest mass exchange between the two phases. Three cases are presented. The first corresponds to passive particles, with a typical beta-like shape and non negligible PDF for relatively large values of vapor $Y_w > 1.5 \times 10^{-3}$. The second corresponds to the active model results in the case of a slow growing process (large initial Knudsen number), and the third curve corresponds to a fast growing process

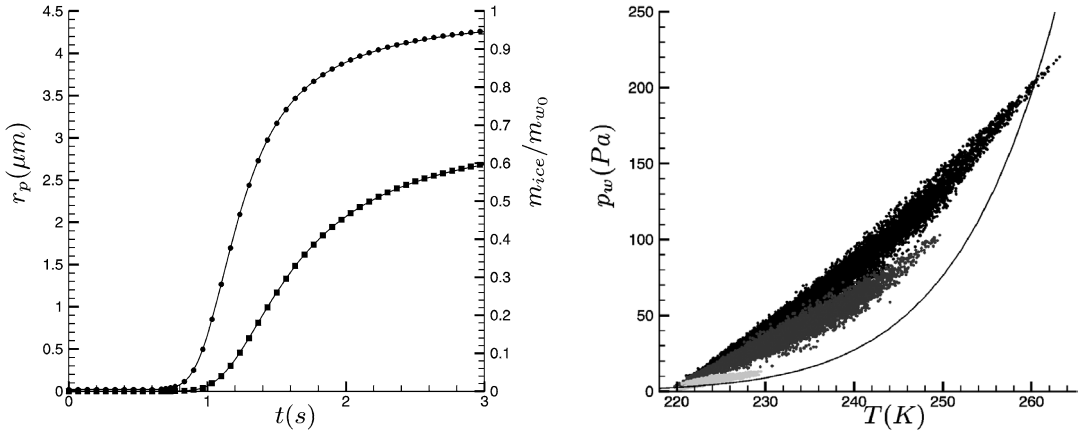

Fig. 20. (a) Evolution of particle mean radius, r_p^{mean} (□), and total ice mass normalized by the initial water vapor content, m_{ice}/m_{w_0} (°); (b) Scatter plot of temperature T and vapor partial pressure p_w around particles at different times from the emission: black dots, $t = 1.4$ s; dark grey, $t = 1.7$ s; light grey, $t = 3$ s (from [85]).

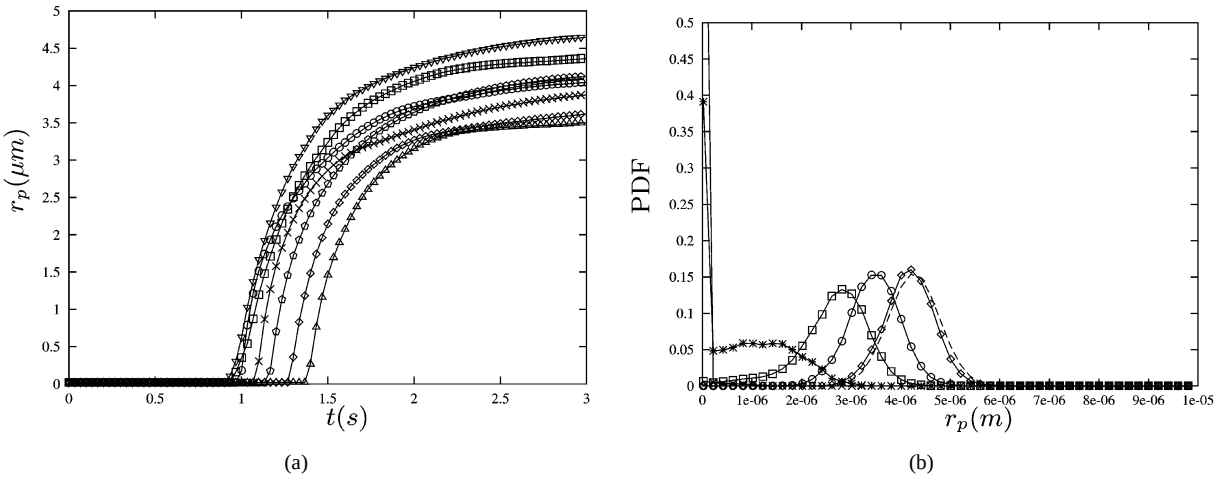

Fig. 21. (a) Time histories of sample particles radii; (b) PDF of particles radius during the interaction phase; $\times$, $t = 0.7$ s; $*$, $t = 1$ s; $\square$, $t = 1.4$ s; $\bigcirc$, $t = 1.7$ s; $\diamondsuit$, $t = 3$ s; dashed line, $t = 3$ s Gaussian (from [85]).

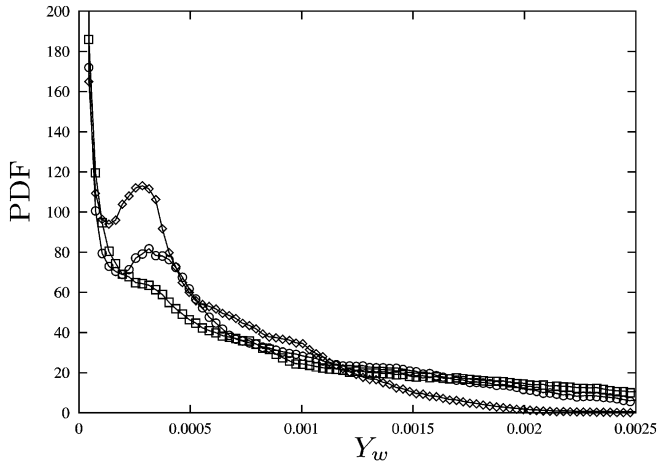

Fig. 22. PDF of water vapor field over the entire domain at $t = 1.7$ s: $\square$, passive tracers; $\bigcirc$, $Kn(0) = 36$; $\diamondsuit$, $Kn(0) = 2.5$ (from [85]).

(low initial Knudsen number). The figure shows the occurrence of a large transport of vapor mass by phase exchange from $Y_w > 1.5 \times 10^{-3}$ to the lower values around $Y_w \simeq 3 \times 10^{-4}$, as confirmed by the appearance of a peak in the PDF (weaker in the case of higher Knudsen because of the slower ice growth). Fig. 22 demonstrates that the freezing of vapor surrounding the large ice particles, illustrated in Fig. 20, directly affects the vapor content which is still available for the other particles. This full-coupling process explains the radii polydispersion.

4. Summary and conclusions

We have presented numerical results of the interaction between exhaust jets and trailing vortices, based on direct numerical simulations (DNS) and large-eddy simulations (LES) approaches. We reviewed recent studies carried out on this topic and described the key physical mechanisms that identify small-scale dynamics and mixing in simple academic configurations, such as between a jet and a single wake vortex.

Based on non-dimensional parameters provided by a wind tunnel experiment, the results of this analysis indicate that the interaction process is mainly controlled by entrainment of the jet by the vortex flow and the turbulent diffusion of the jet. In particular, an instability mechanism was identified, which is due to the injection of axial flow perturbations wrapping around the core itself. This leads to the formation of coherent secondary vorticity structures that enclosed the primary vortex. A strong decay of angular momentum and diffusion of the core is observed only in the case the jet blows inside the vortex core. If the jet

and the vortex are initially well separated, the solid-body rotation of the core prevents passive scalar from penetrating inside the vortex, which also affects mixing with ambient air. This has an impact on the dilution of exhaust species in the atmosphere for which two environmental applications were presented: the chemical conversions of NO_x and the formation and early evolution of a condensation trail in the near field of an aircraft wake. A simple microphysics model which assumes condensation of water vapor directly into ice was integrated in the two-phase flow LES solver (i.e. nucleation and freezing of liquid surfaces were neglected). The analysis showed that the maximum NO_x losses are smaller than an order of 10% of the emitted mixing ratio. Due to the short lifetime of the chemical reactions, these results should not be sensitive to the evolution of temperature and mixing ratio profiles along the wake, because it is limited by OH, which rapidly decreases downstream of the exhaust exit. The next step would be to improve our knowledge of all the chemical mechanisms by means of laboratory work, although the limited local observations made so far in the near field of aircraft wakes do not demonstrate a strong disappearance of NO_x.

Furthermore, when the process of microphysics is analysed, the results showed that the large-scale entrainment of the exhaust by the wake vortex favors vapor condensation due to the increased cooling. Furthermore, accounting for phase coupling provides the deviation from pure mixing in the $T - p_w$ thermodynamic plane, due to vapor removal by condensation. In particular, each crystal grows according to the local supersaturation encountered along its own trajectory in the wake, which ultimately leads to polydispersion of ice-particle radii.

Acknowledgements

The support of COS (Comité d'Orientation sur le Supersonique) is gratefully acknowledged.

References

[1] P.R. Spalart, Airplane trailing vortices, Annu. Rev. Fluid Mech. 30 (1998) 107.
[2] Intergovernmental Panel of Climate Change, Aviation and the Global Atmosphere, Cambridge University Press, Cambridge, UK, 1999.
[3] D.W. Fahey, U. Schumann, Aviation-produced aerosols and cloudiness, in: J.E. Penner et al. (Eds.), Aviation and the Global Atmospheren, International Panel of Climate Change, Special Report.
[4] P. Schulte, H. Schlager, H. Ziereis, U. Schumann, S.L. Baughcum, F. Deidewig, NO_x emission indices of subsonic long-range jet aircraft at cruise altitude: in situ measurements and predictons, J. Geophys. Res. 102 (1997) 21 431–21 442.
[5] U. Schumann, H. Schlager, F. Arnold, R. Baumann, P. Haschberger, O. Klemm, Dilution of aircraft exhaust plumes at cruise altitudes, Atmos. Environ. 32 (1998) 3097–3103.
[6] F. Garnier, C. Baudoin, P. Woods, N. Louisnard, Engine emission alteration in the near field of an aircraft, Atmos. Environ. 31 (1997) 1767–1781.
[7] T. Gerz, T. Durbeck, P. Konopka, Transport and effective diffusion of aircraft emissions, J. Geophys. Res. 103 (1998) 25 905–25 913.
[8] H. Hoshizaki, L.B. Anderson, R.J. Conti, N. Farlow, J.W. Meyer, T. Overcamp, K.O. Redler, V. Watson, in: CIAP Monograph 3, The Stratosphere Perturbed by Propulsion Effluents, Final Report-DOT-TST-75-53, U.S. Department of Transportation, Washington, DC, 1975.
[9] R.C. Miake-Lye, R.C. Brown, C.E. Kolb, Plume and wake dynamics, mixing and chemistry behind a high speed civil transport aircraft, J. Aircraft 30 (1993) 467–479.
[10] Z. El-Ramy, W.J. Rainbird, Effect of simulated jet engines on the flowfield behind a swept-back wing, J. Aircraft 14 (1977) 343–349.
[11] S. Brunet, F. Garnier, L. Jacquin, Numerical/experimental simulation of exhaust jet mixing in wake vortex, AIAA paper 1999-3418, 1999.
[12] J.M. Seiner, M.K. Ponton, B.J. Jansen S.M. Dash, D.C. Kenakowski, Installation effects on high speed plume evolution, ASME paper FEDSM97-3227, 1997.
[13] F.Y. Wang, M.J. Proot, J.-M. Charbonnier, Near-field interaction of a jet with leading-edge vortices, J. Aircraft 37 (2000) 779–785.
[14] F.Y. Wang, K.B.M.Q. Zaman, Aerodynamic of a jet in the vortex-wake of a wing, AIAA J. 40 (2002) 401–407.
[15] H.L. Kantha, W.S. Lewellen, F.H. Durgin, Response of a trailing vortex to axial injection into the core, J. Aircraft 9 (1972) 226–254.
[16] W.R.C. Phillips, J.A.H. Graham, Reynolds stress measurements in a turbulent trailing vortex, J. Fluid Mech. 147 (1984) 353–371.
[17] G. Huppertz, E. Fares, R. Abstiens, W. Schroder, Investigation of engine jet/wing-tip vortex interference, Aerosp. Sci. Tech. 8 (2004) 175–183.
[18] E. Fares, M. Meinke, W. Schroeder, Numerical simulation of the interaction of wingtip vortices and engine jets in the near field, AIAA paper 2000-2222, 2000.
[19] T. Gerz, T. Ehret, Wingtip vortices and exhaust jets during the jet regime of aircraft wakes, Aerosp. Sci. Tech. 1 (1997) 463–474.
[20] F. Garnier, S. Brunet, L. Jacquin, Modeling exhaust plume mixing in the near field of an aircraft, Ann. Geophys. 16 (1997) 1468–1477.
[21] T. Gerz, F. Holzapfel, Wingtip vortices, turbulence, and the distribution of emissions, AIAA J. 37 (1999) 1270–1276.
[22] F. Holzapfel, T. Gerz, D. Darracq, H. Moet, F. Garnier, C. Ferreira Gago, Analysis of wake vortex decay mechanisms in the atmosphere, Aerosp. Sci. Tech. 7 (2003) 263–275.
[23] A. Michalke, G. Hermann, On the inviscid instability of a circular jet with external flow, J. Fluid Mech. 114 (1982) 343–359.
[24] P. Brancher, Etude numérique des instabilités secondaires de jets, Ph.D. thesis, Ecole Polytechnique, Palasieu, 1996.
[25] T. Loiseleux, J.M. Chomaz, P. Huerre, The effects of swirl on jets and wakes: Linear instability of the Rankine-vortex with axial vortex, Phys. Fluids 10 (1998) 1120–1134.

[26] G. Lu, S.K. Lele, Inviscid instability of compressible swirling mixing layers, Phys. Fluids 11 (1999) 450–461.
[27] J.B. Freund, S.K. Lele, P. Moin, Compressibility effects in a turbulent annular mixing layer. Part 1. Turbulence and growth rates, J. Fluid Mech. (2000) 229–267.
[28] J.B. Freund, P. Moin, S.K. Lele, Compressibility effects in a turbulent annular mixing layer. Part 2. Mixing of a passive scalar, J. Fluid Mech. (2000) 269–292.
[29] J.B. Freund, S.K. Lele, P. Moin, Numerical simulation of a Mach 1.92 turbulent jet and its sound field, AIAA J. 38 (2000) 2023–2031.
[30] J.B. Freund, Noise sources in a low-Reynolds-number turbulent jet at Mach 0.9, J. Fluid Mech. (2001) 277–305.
[31] F.P. Ricou, D.B. Spalding, Measurements of entrainment by axisymmetrical turbulent jets, J. Fluid Mech. 11 (1961) 21–32.
[32] G.N. Abramovich, O.V. Yakovleski, I.P. Smirnova, A.N. Secundov, S. Yu, An investigation of the turbulent jets of different gases in a general stream, Acta Astron. 14 (1969) 229.
[33] P.A. Monkewitz, X.D. Sohn, Absolute instability in hot jets, AIAA J. 26 (1988) 911–916.
[34] V.J. Rossow, Lift-generated vortex wakes of subsonic transport aircraft, Prog. Aerosp. Sci. 35 (1999) 507.
[35] G. Batchelor, Axial flow in trailing line vortices, J. Fluid Mech. 20 (1964) 645–658.
[36] E.W. Mayer, K.G. Powell, Viscous and inviscid instabilities of a trailing vortex, J. Fluid Mech. 245 (1992) 91–114.
[37] S. Ragab, M. Sreedhar, Numerical simulation of vortices with axial velocity deficits, Phys. Fluids 7 (1995) 549–558.
[38] G. Hu, D. Sun, X. Yin, A numerical study of dynamics of a temporally evolving swirling jet, Phys. Fluids 13 (2001) 951–965.
[39] D.C. Lewellen, W.S. Lewellen, Large-eddy simulations of the vortex-pair breakup in aircraft wakes, AIAA J. 34 (1996) 2337–2345.
[40] D.C. Lewellen, W.S. Lewellen, L.R. Poole, R.J. DeCoursey, G.M. Hansen, C.A. Hostetler, G.S. Kent, Large-eddy simulations and lidar measurements of vortex-pair breakup in aircraft wakes, AIAA J. 36 (1998) 1439–1445.
[41] S.C. Rennich, S.K. Lele, Method for accelerating the destruction of aircraft wake vortices, J. Aircraft 36 (1999) 398–404.
[42] T. Leweke, C.H.K. Williamson, Cooperative elliptic instability of a vortex pair, J. Fluid Mech. 360 (1998) 85–119.
[43] S. Le Dizès, F. Laporte, Theoretical predictions for the elliptic instability in a two-vortex flow, J. Fluid. Mech. 471 (2002) 169–201.
[44] J.D. Crouch, Instability and transient growth for two trailing-vortex pairs, J. Fluid Mech. 350 (1997) 311–330.
[45] D. Fabre, L. Jacquin, Stability of a four-vortex aircraft wake model, Phys. Fluids 12 (2000) 2438–2443.
[46] W.J. Devenport, M.C. Rife, S.I. Liapis, G.J. Follin, The structure and development of a wing-tip vortex, J. Fluid Mech. 312 (1996) 67–106.
[47] W.J. Devenport, J.S. Zsoldos, C.M. Vogel, The structure and development of a counter-rotating wing-tip vortex pair, J. Fluid Mech. 332 (1997) 1–104.
[48] A. Chen, J.D. Jacob, O. Savas, Dynamics of corotating vortex pairs in the wakes of flapped airfoils, J. Fluid Mech. 382 (1999) 155–193.
[49] L. Jacquin, D. Fabre, P. Geffroy, E. Coustols, The properties of a transport aircraft wake in the extended near field: an experimental study, AIAA paper 2001-1038, 2001.
[50] D. Fabre, Instabilités et instationnarités dans les tourbillons: application aux sillage d'avions, Ph.D. thesis, Université Paris VI – ONERA, 2002.
[51] F. Laporte, Simulation numérique appliquée à la caractérisation et aux instabilités des tourbillons de sillage d'avions de transport, Ph.D. thesis, Institut National Polytechnique de Toulouse – CERFACS, 2002.
[52] C. Ferreira Gago, S. Brunet, F. Garnier, Numerical investigation of turbulent mixing in a jet/wake vortex interaction, AIAA J. 40 (2002) 276–284.
[53] R. Paoli, F. Laporte, B. Cuenot, T. Poinsot, Dynamics and mixing in jet/vortex interactions, Phys. Fluids 15 (2003) 1843–1860.
[54] S.K. Lele, Compact finite difference scheme with spectral-like resolution, J. Comp. Phys. 103 (1992) 16–42.
[55] T. Poinsot, S.K. Lele, Boundary conditions for direct simulations of compressible viscous flows, J. Comp. Phys. 101 (1992) 104–129.
[56] M. Gaster, A note on the relation between temporally-increasing and spatially-increasing disturbances in hydrodynamic stability, J. Fluid Mech. 14 (1962) 222–224.
[57] R. Verzicco, P. Orlandi, Direct simulations of the transitional regime of a circular jet, Phys. Fluids 6 (1994) 751–759.
[58] A.B. Cortesi, B.L. Smith, G. Yadigaroglu, S. Banerjee, Numerical investigation of the entrainment and mixing processes in neutral and stably-stratified mixing layers, Phys. Fluids 7 (1999) 162–184.
[59] S. Brunet, L. Jacquin, P. Geffroy, Experimental heated jets/wake vortex interaction, ONERA Report RT 15/2496 DAFE/Y, 1999.
[60] P.G. Saffman, Vortex Dynamics, Cambridge University Press, Cambridge, UK, 1992.
[61] G. Erlebacher, M.Y. Hussaini, C.G. Speziale, T.A. Zang, Towards the large-eddy simulation of compressible turbulence, J. Fluid Mech. 238 (1992) 155–185.
[62] P. Moin, K. Squires, W. Cabot, S. Lee, A dynamic subgrid-scale model for compressible turbulence and scalar transport, Phys. Fluids 3 (1991) 2746–2757.
[63] F. Ducros, P. Comte, M. Lesieur, Large-eddy simulation of transition to turbulence in a boundary layer spatially developing over a flat plate, J. Fluid. Mech. 326 (1996) 1–36.
[64] O. Métais, M. Lesieur, Spectral large-eddy simulation of isotropic and stably stratified turbulence, J. Fluid. Mech. 239 (1992) 157–194.
[65] L. Jacquin, C. Pantano, On the persistence of trailing vortices, J. Fluid Mech. 471 (2002) 159–168.
[66] J. Jeong, F. Hussain, On the identification of a vortex, J. Fluid Mech. 285 (1995) 69–94.
[67] B.M. Cetegen, N. Mohamad, Experiments on liquid mixing and reaction in a vortex, J. Fluid Mech. 249 (1993) 391–414.
[68] W.B. De More, S.P. Sander, D.M. Golden, M.J. Molina, R.F. Hampson, M.J. Kuylo, C.J. Howard, A.R. Ravihankara, Chemical Kinetics and Photo-Chemical Data for Use in Stratospheric Modeling, JPL Publication, 1992.
[69] World Meteorological Organization, Scientific assessment of ozone depletion, Global Ozone Research and Monitoring Project, Report 25, 1992.
[70] S.K. Meilinger, B. Kärcher, T. Peter, Suppression of chlorine activation on aviation-produced volatile particles, Atmos. Chem. Phys. 2 (2002) 307–312.

[71] W.R. Stockwell, J.G. Calvert, The mechanism of the HO–SO_2 reaction, Atmos. Environ. 17 (1983) 2231–2235.
[72] F. Arnold, J. Scheid, T. Stilp, H. Schlager, E. Reinhardt, Measurements of jet aircraft emissions at cruise altitude I: the odd-nitrogen gases NO, NO_2 and HNO_3, Geophys. Res. Lett. 19 (1992) 2421–2424.
[73] T. Reiner, F. Arnold, Laboratory flow reactor measurements of reaction $SO_3 + H_2O + M \rightarrow H_2SO_4$: implication for gaseous H_2SO_4 and aerosol formation in the plume of the jet aircraft, Geophys. Res. Lett. 20 (1993) 2659–2662.
[74] A.M. Starik, A.M. Savel'ev, N.S. Titova, U. Schumann, Modeling of sulfur gases and chemiions in aircraft engines, Aerosp. Sci. Techn. 6 (2002) 63–81.
[75] A.M. Starik, A.M. Savel'ev, N.S. Titiva, E.E. Loukhovitskaya, U. Schumann, Effect of aerosol precursors from gas turbine engines on the volatile sulfate aerosols and ion clusters formation in aircraft plumes, Phys. Chem. Chem. Phys. 6 (2004) 3426–3436.
[76] A. Sorokin, E. Katragkou, F. Arnold, R. Busen, U. Schumann, Gaseous SO_3 and H_2SO_4 in the exhaust of an aircraft gas turbine engine: measurements by CIMS and implications for fuel sulfur conversion to sulfur (VI) and conversion of SO_3 to H_2SO_4, Atmos. Environ. 38 (2004) 449–456.
[77] H. Appleman, The formation of exhaust condensation trails by jet aircraft, Bull. Amer. Meteor. Soc. 34 (1953) 14–20.
[78] U. Schumann, On the conditions for contrails formation, Meteorol. Z. 5 (1996) 4–23.
[79] A. Petzold, R. Busen, F. Schröder, R. Baumann, M. Kuhn, D.E. Hagen, P.D. Whitefield, D. Baumgardner, F. Arnold, S. Borrmann, U. Schumann, Near-field measurements on contrail properties from fuels with different sulfur content, J. Geophys. Res. 102 (1997) 29 867–29 881.
[80] F. Schröder, B. Kärcher, C. Duroure, J. Ström, A. Petzold, J.-F. Gayet, B. Strauss, P. Wendling, S. Borrmann, On the transition of contrails into cirrus, J. Atmos. Sci. 57 (2000) 464–480.
[81] U. Schumann, F. Arnold, R. Busen, J. Curtius, B. Kärcher, A. Kiendler, A. Petzold, H. Schlager, F. Schröder, K.-H. Wohlfrom, Influence of fuel sulfur on the composition of aircraft exhaust plumes: the experiments SULFUR 1-7, J. Geophys. Res. 107 (D15) (2002) AAC 2-1–AAC 2-27, 10.1029/2001JD000813.
[82] R. Sussmann, K. Gierens, Lidar and numerical studies of the different evolution of vortex pair and secondary wake in young contrails, J. Geophys. Res. 104 (1999) 2131–2142.
[83] D.C. Lewellen, W.S. Lewellen, The effects of aircraft wake dynamics on contrail development, J. Atmos. Sci. 58 (2001) 390–406.
[84] K.M. Gierens, Numerical simulations of persistent contrails, J. Atmos. Sci. 53 (1996) 3333–3348.
[85] R. Paoli, J. Hélie, T. Poinsot, Contrail formation in aircraft wakes, J. Fluid Mech. 502 (2004) 361–373.
[86] P. Mirabel, F. Garnier, J.-F. Gayet, R. Sussmann, J. Strom, P. Wendling, Formation processes and radiative properties of particles in aircraft wakes, Aerocontrail Final report, 1998.
[87] R. Paoli, J. Hélie, T. Poinsot and S. Ghosal, Contrails formation in aircraft wakes using large-eddy simulations, in: Proc. Summer Program of the Center for Turbulence Research, Stanford, 2002, pp. 229–241.
[88] M. Boivin, O. Simonin, K.D. Squires, Direct numerical simulations of turbulence modulation by particles in isotropic turbulence, J. Fluid Mech. 375 (1998) 235–263.
[89] P.K. Yeung, S.B. Pope, An algorithm for tracking fluid particles in numerical simulations of homogeneous turbulence, J. Comp. Phys. 79 (1988) 373–416.
[90] B. Karcher, T. Peter, U. Biermann, U. Schumann, The initial composition of jet condensation trails, J. Atmos. Sci. 53 (1996) 3066–3083.
[91] B. Karcher, Physicochemistry of aircraft-generated liquid aerosols, soot, and ice particles. Part 1. Model description, J. Geophys. Res. 103 (1998) 17111–17128.
[92] B. Karcher, R. Busen, A. Petzold, F.P. Schröder, U. Schumann, E.J. Jensen, Physicochemistry of aircraft-generated liquid aerosols, soot, and ice particles. Part 2. Comparison with observations and sensitivity studies, J. Geophys. Res. 103 (1998) 17 129–17 147.
[93] X. Qu, E.J. Davis, Droplet evaporation and condensation in the near-continuum regime, J. Aerosol Sc. 32 (2001) 861–875.
[94] D. Sonntag, Advancements in the field of hygrometry, Meteorol. Z. 3 (1994) 51–66.